Shape dependence of Edelstein and magnetoelectric effects in the V-shaped model

Shuhei Kanda* and Satoru Hayami
Graduate School of Science, Hokkaido University, Sapporo 060-0810, Japan

(Received 18 November 2025; accepted 19 October 2026; published 28 October 2026)

We theoretically investigate the shape dependence and microscopic mechanism of the magnetoelectric (ME) effect, including both nonmagnetic (Edelstein-type) and magnetic origins, in a V-shaped one-dimensional chain model. Numerical calculations based on the Kubo formula reveal that the nonmagnetic-driven ME response is maximized at an apex angle of $\theta \approx 0.6\pi$. To clarify its origin, we derive a low-energy effective Hamiltonian in the s-orbital subspace and demonstrate that the polarity induced by the V-shaped geometry manifests as an effective spin-orbit interaction. An analytical derivation of the Green's function shows that the geometric effect can be described as a T-matrix contribution associated with local symmetry breaking. This scattering-theoretical representation enables us to identify the contributions of local geometric symmetry breaking to the ME response. Using a multipole-basis representation, we identify symmetry-based selection rules for the ME tensor and show that the coupling between the effective spin-orbit interaction and the orbital angular momentum generated across the apex plays an essential role. The resulting angular dependence, $\sin\theta \sin\theta/2$, peaks at $\theta = 2\tan^{-1}\sqrt{2} \approx 0.608\pi$, in good agreement with the numerical results. We also analyze a ferromagnetic V-shaped model including the Zeeman interaction and show that the magnetic-driven ME response originates from the spin magnetization induced by the coupling between the electric-field-driven charge-potential gradient and the Zeeman term. These results reveal distinct ME mechanisms depending on the presence or absence of time-reversal symmetry and clarify the microscopic origin of shape-dependent ME responses in V-shaped chains.

DOI: 10.1103/qjfd-tbyj

I. INTRODUCTION

Artificially structured metamaterials (or metasurfaces) have enabled unprecedented creation and manipulation of physical phenomena [1–5]. In particular, recent advances in microfabrication techniques have made it possible to induce specific symmetries into a system, for example, by fabricating holes of designed shapes [6–8] or by constructing tailored nanostructured architectures [2,9–12]. Similarly, in atomic-scale and nanoscale materials, the control of geometric configurations and atomic arrangements provides opportunities to tailor electronic states and physical properties through structural and symmetry engineering [13–17]. Such artificial systems provide a valuable platform for exploring and realizing exotic physical phenomena, which can be flexibly engineered

*Contact author: kanda@phys.sci.hokudai.ac.jp

Published by the American Physical Society under the terms of the Creative Commons Attribution 4.0 International license. Further distribution of this work must maintain attribution to the author(s) and the published article's title, journal citation, and DOI.

through the geometric parameters of the constituent nanostructures, including their composition, shape, periodicity, and mutual arrangement.

To systematically characterize the symmetry and associated physical responses of such artificially engineered systems, it is useful to adopt a symmetry-based theoretical framework. The finite multipole moments in a system reflect its underlying symmetry. The multipole description provides a powerful way to connect macroscopic phenomena, microscopic degrees of freedom, and symmetry principles [18–24]. Microscopic internal degrees of freedom, such as spin, orbital, and charge, can be systematically classified within the multipole basis, which provides a complete set for describing arbitrary electronic states in a given Hilbert space [18,22,24,25]. Consequently, extensive studies have been devoted to macroscopic response phenomena originating from bulk electronic degrees of freedom using multipole basis. These efforts have employed the multipole basis to extract key model parameters and to characterize the resulting emergent behaviors [22–24,26].

Meanwhile, the detailed correspondence between the symmetries induced by nanoscale geometries and the multipole degrees of freedom remains unclear, beyond the level of symmetry classification [19,21,24]. For example, it is still unclear how local geometric structures affect electronic states and through what microscopic mechanisms they influence macroscopic physical properties. Elucidating the interplay between nanoscale geometries and multipole degrees of freedom may provide valuable insights into the understanding and design of geometry-induced electronic properties in nanostructures.

We focus on a V-shaped (so-called "ku-noji"-shaped in Japanese) structure [27–31], which possesses C_{2v} (m2m) symmetry or C_s (m) symmetry when the substrate is taken into account. In such metamaterials, the shape-induced polarity gives rise to a finite electric dipole moment, which becomes the microscopic origin of the Edelstein effect [32–35], the nonlinear Hall effect [23,36–39], the nonlinear optical response [40–43], and the piezoelectric effect [44–46]. Furthermore, in ferromagnetic V-shaped systems, magnetic dipole degrees of freedom originating from spontaneous magnetization become active, leading to a multiferroic state that simultaneously breaks time-reversal and spatial-inversion symmetries. In such multiferroics, magnetic toroidal dipole degrees of freedom, which are characterized by polar vectors that are odd under time-reversal symmetry [18,24,47–49], play an essential role. These toroidal moments give rise to rich physical phenomena such as magnetoelectric (ME) effects [47,48,50–56], nonreciprocal conductivity [55,57–59], and nonreciprocal directional dichroism [12,60–62].

In this paper, we investigate the shape dependence and the underlying mechanism of the ME response arising from the V-shaped geometry using a one-dimensional (1D) chain model; hereafter, the term "ME effect" is used in a generalized sense to refer collectively to the nonmagnetic-driven Edelstein effect associated with electric dipoles and the magnetic-driven ME response induced by magnetic toroidal dipoles. The finite V-shaped chain serves as a minimal microscopic model for examining local geometric symmetry breaking, rather than a material-specific description of a bulk crystal or a mesoscopic device. Here, we aim to clarify how local geometric symmetry breaking is encoded in ME responses from a microscopic viewpoint. First, we evaluate the shape dependence of the nonmagnetic-driven ME effect in a model including s and p orbitals. We find that the magnitude of the ME effect reaches its maximum at an apex angle of $\theta \approx 0.6\pi$. To analyze the mechanism underlying this dependence, we next perform a more detailed model analysis. By projecting onto the s-orbital basis, we construct a low-energy effective Hamiltonian, in which the polarity induced by the V-shaped geometry emerges as an effective spin-orbit interaction. Furthermore, by analyzing the shape dependence of the Green's function, we clarify that the geometric effect manifests itself as a T-matrix contribution to the Green's function. We then analyze the selection rules using the multipole basis, which reveals that the effective spin-orbit interaction and the orbital angular momentum generated by motion across the apex angle play essential roles in the ME effect. The angular dependence of this mechanism takes the form $\sin\theta \sin\theta/2$, exhibiting a peak around $\theta = 2\tan^{-1}\sqrt{2} \approx 0.608\pi$, demonstrating that the observed shape dependence is a direct consequence of the underlying microscopic mechanism. Finally, we investigate a V-shaped ferromagnetic model including Zeeman interaction. We find that the magnetic-driven ME effect in this case arises from

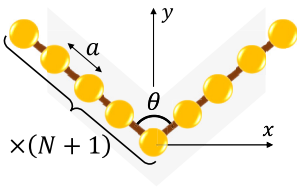


FIG. 1. The lattice of the $2N + 1$-site ($N = 4$) V-shaped 1D chain defined in Eq. (2). a is the lattice constant and θ is the apex angle.

spin magnetization induced by the coupling between the charge-potential gradient generated by the V-shaped geometry and the Zeeman interaction. These distinct physical mechanisms result in different dependence of the ME effect on both shape and system size. These results provide microscopic insights into the relationship between local geometric symmetry breaking and ME responses in V-shaped nanostructures.

The organization of this paper is as follows. In Sec. II, we present the numerical results demonstrating the shape dependence of the nonmagnetic-driven ME effect in a model including s and p orbitals. In Sec. III, we derive an effective Hamiltonian and show that the polarity induced by the V-shaped geometry results in the effective spin-orbit interaction. In Sec. IV, we analyze the shape dependence of the Green's function. In Sec. V, we employ the multipole basis to analyze the selection rules for the ME tensor, thereby clarifying the key physical mechanisms underlying the shape dependence. In Sec. VI, we further investigate the shape dependence and the underlying mechanism of the magnetic-driven ME effect in a ferromagnetic system without the time-reversal symmetry. Section VII is devoted to the summary of the present findings. Appendixes include the derivation of the Green's function of the straight 1D chain in Appendix A, the matrix representation of multipoles in the V-shaped model in Appendix B, and the expression of the ME tensor based on the multipole basis in Appendix C.

II. *s-p* MODEL

We evaluate the shape dependence of the ME effect in a model including s and p orbitals. In Sec. II A, we introduce the s-p-orbital model in the V-shaped chain system. We also show the expression of the linear ME tensor, which describes the correlation between the electric polarization and the magnetization in Sec. II B.

A. Model and method

We consider a minimal model of a V-shaped finite chain on the xy plane that captures the essential symmetry and orbital structure, incorporating s and p orbitals, as shown in Fig. 1. The tight-binding Hamiltonian is given by

$$H = \sum_{\boldsymbol{R}_n \boldsymbol{R}_{n'}} \sum_{mm'\sigma\sigma'} \varphi^{\dagger}_{m\sigma}(\boldsymbol{R}_n)\, h^{nn'}_{mm'\sigma\sigma'}\, \varphi_{m'\sigma'}(\boldsymbol{R}_{n'}), \tag{1}$$

where $\varphi_{m\sigma}(\boldsymbol{R}_n)$ and $\varphi^{\dagger}_{m\sigma}(\boldsymbol{R}_n)$ are the fermionic annihilation and creation operators of the s-p orbital $m = s, p_x, p_y, p_z$, the spin $\sigma = \uparrow, \downarrow$, and the position $\boldsymbol{R}_n$. The V-shaped 1D chain lattice consists of the $2N + 1$ sites, whose positions are specified by $\boldsymbol{R}_n$ defined as

$$\boldsymbol{R}_n = a\left(n \sin\frac{\theta}{2}, |n| \cos\frac{\theta}{2}\right) \quad (-N \leqslant n \leqslant N), \tag{2}$$

where a is the lattice constant and θ is the apex angle of the V shape, as shown in Fig. 1.

The Hamiltonian is decomposed into three parts as follows:

$$H = H_{\rm hop} + H_{\Delta} + H_{\rm SOC}. \tag{3}$$

The first term $H_{\rm hop}$ represents the hopping term, which includes the Slater-Koster parameters $t_{ss\sigma}$ and $t_{sp\sigma}$ for the nearest-neighbor hopping [63]. The hopping between the p orbitals is neglected ($t_{pp\sigma} = t_{pp\pi} = 0$) for simplicity. $H_{\rm hop}$ is given by

$$H_{\rm hop} = \sum_{\boldsymbol{R},\boldsymbol{\delta}} \sum_{mm'\sigma} \varepsilon_{\boldsymbol{\delta},mm'}\, \varphi^{\dagger}_{m\sigma}(\boldsymbol{R} + a\boldsymbol{\delta})\, \varphi_{m'\sigma}(\boldsymbol{R}), \tag{4}$$

where the lattice number n of $\boldsymbol{R}_n$ is omitted for notational simplicity (e.g., $\boldsymbol{R} = \boldsymbol{R}_n$, $\boldsymbol{\delta} = \boldsymbol{\delta}_n$). $\boldsymbol{\delta}$ is the direction cosine for the nearest-neighbor sites from $\boldsymbol{R}$. The relationship between ε and the Slater-Koster parameters is given by

$$\varepsilon_{\boldsymbol{\delta},ss} = -t_{ss\sigma}\,, \quad \varepsilon_{\boldsymbol{\delta},sp_i} = -\varepsilon_{\boldsymbol{\delta},p_i s} = t_{sp\sigma}\delta^{i} \quad (i = x, y), \quad \varepsilon_{\boldsymbol{\delta},mm'} = 0 \quad \text{(otherwise)}. \tag{5}$$

The second term H_{Δ} represents the energy level of the p orbital measured from that of the s orbital, which is expressed as

$$H_{\Delta} = \Delta_p \sum_{\boldsymbol{R}} \sum_{m\sigma}^{m=p_x,p_y,p_z} \varphi^{\dagger}_{m\sigma}(\boldsymbol{R})\, \varphi_{m\sigma}(\boldsymbol{R}). \tag{6}$$

The third term $H_{\rm SOC}$ represents the atomic spin-orbit coupling (SOC) term, which is represented by

$$H_{\rm SOC} = \frac{2\lambda}{\hbar^2} \sum_{\boldsymbol{R}} \sum_{mm'\sigma\sigma'} \boldsymbol{l}_{mm'} \cdot \boldsymbol{s}_{\sigma\sigma'}\, \varphi^{\dagger}_{m\sigma}(\boldsymbol{R})\, \varphi_{m'\sigma'}(\boldsymbol{R}), \tag{7}$$

where $\boldsymbol{l}_{mm'}$ and $\boldsymbol{s}_{\sigma\sigma'}$ represent the matrix elements of the orbital and spin angular momentum operators, respectively. $\hbar$ is the reduced Planck constant. It is noted that the orbital angular momentum operator is defined within the p-orbital subspace.

For the above model, we evaluate the ME tensor by using the linear response theory. The ME tensor $\alpha^{\nu;\rho}$, which corresponds to the coefficient describing the linear response of the magnetization δM^{ν} to an external electric field E^{ρ}, is defined as

$$\delta M^{\nu} = \sum_{\rho} \alpha^{\nu;\rho} E^{\rho}. \tag{8}$$

Within the framework of linear response theory, the ME tensor incorporates contributions from the Edelstein effect with the dissipation, which preserves time-reversal symmetry, and from the conventional ME effect without the dissipation, which requires its breaking [19–21,24]. In the V-shaped model preserving time-reversal symmetry, the point-group symmetry of the system is $C_{2\rm v}$ owing to the emergence of electric polarization along the y direction. This polar symmetry allows a finite $\alpha^{z;x}$ component in two-dimensional systems.

We calculate the linear ME tensor using the Kubo formula:

$$\alpha^{\nu;\rho} = -\frac{1}{V} \sum_{AB} \frac{f(E_A) - f(E_B)}{E_A - E_B + i\hbar\gamma} M^{\nu}_{AB} P^{\rho}_{BA}, \tag{9}$$

where E_A are the eigenvalues of Hamiltonian matrix $\bar{h}$, $f(E)$ is the Fermi distribution function, $V = (2N+1)a$ is the volume of the system, and γ is the scattering rate, characterized as the inverse of the relaxation time under the relaxation time approximation. M^{ν}_{AB} and P^{ρ}_{BA} are matrix elements of the magnetization and polarization operators for eigenstates A and B, respectively. Their operator

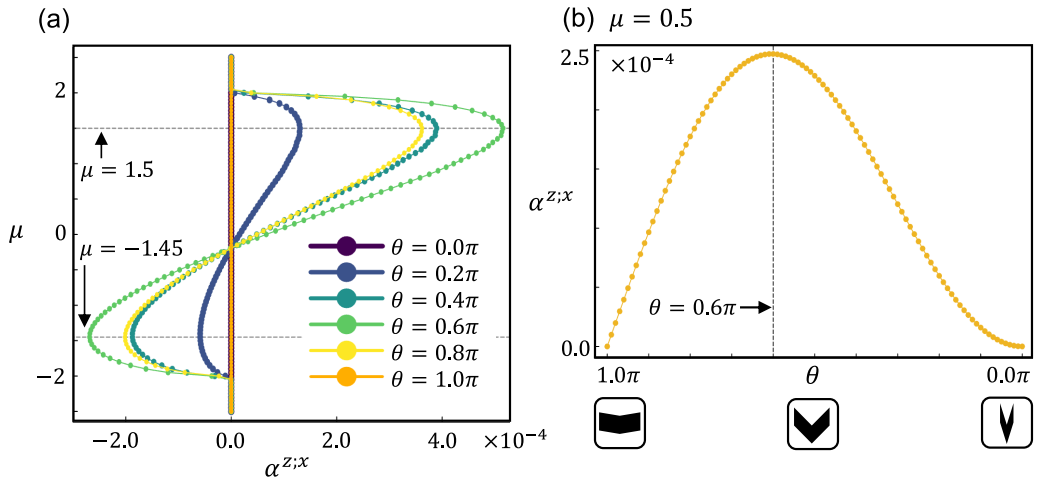


FIG. 2. (a) Chemical potential μ dependence of the nonmagnetic-driven ME tensor component $\alpha^{z;x}$ for various apex angles, $\theta = 0.0\pi, 0.2\pi, \ldots, 1.0\pi$. $\alpha^{z;x}$ reaches its maximum around $\mu \approx 1.5$ and its minimum around $\mu \approx -1.45$, independent of the value of θ. (b) Apex angle θ dependence of the ME tensor at $\mu = 0.5$. The magnitude of the ME response induced by the V-shaped geometry reaches its maximum at $\theta \approx 0.6\pi$. In both panels (a) and (b), the parameters are set to $t_{ss\sigma} = 1$, $t_{sp\sigma} = 0.7$, $\Delta_p = 10$, $\lambda = 0.4$, $N = 128$, $\gamma = 0.05$, and $T = 0.01$.

expressions are given by

$$M^{\nu} = \frac{\mu_{\mathrm{B}}}{\hbar}(L^{\nu} + gS^{\nu}), \tag{10}$$

$$L^{\nu} = \sum_{\boldsymbol{R}} \sum_{mm'\sigma} l^{\nu}_{mm'} \varphi^{\dagger}_{m\sigma}(\boldsymbol{R}) \varphi_{m'\sigma}(\boldsymbol{R}), \tag{11}$$

$$S^{\nu} = \sum_{\boldsymbol{R}} \sum_{m\sigma\sigma'} s^{\nu}_{\sigma\sigma'} \varphi^{\dagger}_{m\sigma}(\boldsymbol{R}) \varphi_{m\sigma'}(\boldsymbol{R}), \tag{12}$$

$$P^{\rho} = e \sum_{\boldsymbol{R}} \sum_{m\sigma} R^{\rho} \varphi^{\dagger}_{m\sigma}(\boldsymbol{R}) \varphi_{m\sigma}(\boldsymbol{R}), \tag{13}$$

where e, μ_{B}, and g are the elementary charge, the Bohr magneton, and the g factor, respectively. We neglect the additional contribution from the modern theory of orbital magnetization [64,65] and interorbital polarization [66].

B. Numerical results

We evaluate the shape dependence of the ME tensor $\alpha^{z;x}$ in the V-shaped s-p model as Eq. (3). In the following numerical calculations in this subsection, we set

$$t_{ss\sigma} = 1, \quad t_{sp\sigma} = 0.7, \quad \Delta_p = 10, \quad \lambda = 0.4, \tag{14}$$

and $N = 128$. We also set $e = \hbar = \mu_{\mathrm{B}} = a = 1$, $g = 2$, $\gamma = 0.05$, and the temperature $T = 0.01$. Since we consider the nonmagnetic system with time-reversal symmetry, the ME response $\alpha^{z;x}$ becomes nonzero only under the finite dissipation.

First, we present the chemical potential μ dependence for various apex angles θ. We focus on the range $-2 \leqslant \mu \leqslant 2$, in which the electronic states are primarily characterized by the s orbital owing to the large energy separation Δ_p. As shown in Fig. 2(a), $\alpha^{z;x}$ reaches its maximum around $\mu \approx 1.5$ and its minimum around $\mu \approx -1.45$, independent of the value of θ. The disappearance of $\alpha^{z;x}$ for $\theta = \pi$ is owing to the presence of the spatial-inversion symmetry, where the system

reduces to the straight 1D chain. Meanwhile, the vanishing of $\alpha^{z,x}$ at $\theta = 0$ implies that a finite opening along the x direction in the V-shaped geometry, which results in the x-directional electric polarization, is essential for the nonmagnetic-driven ME effect. These results also suggest that, in the present model, the characteristic shape dependence of the ME response is not restricted to a particular chemical potential.

Figure 2(b) shows the θ dependence of the ME effect at $\mu = 0.5$. We choose this chemical potential as a representative value away from the extrema of the ME response. This choice is not based on any specific material or electron filling. The magnitude of the ME response exhibits a nearly monotonic dependence on θ, showing a clear peak at an apex angle of approximately $\theta \approx 0.6\pi$. This behavior is clarified by employing the approach based on an effective model in the subsequent section.

III. EFFECTIVE MODEL

To analyze the underlying physical mechanism of the numerically obtained ME response, we adopt an effective model approach that eliminates redundant degrees of freedom to capture the essential physics. To this end, we derive an effective Hamiltonian by projecting the s-p orbital model onto the s-orbital subspace [67–70]:

$$H_{\rm eff}(z) = \sum_{\boldsymbol{R}_n \boldsymbol{R}_{n'}} \sum_{\sigma\sigma'} \varphi^{\dagger}_{s\sigma}(\boldsymbol{R}_n)[\bar{h}_{\rm eff}(z)]^{nn'}_{\sigma\sigma'}\varphi_{s\sigma'}(\boldsymbol{R}_{n'}), \tag{15}$$

$$\bar{h}_{\rm eff}(z) = \bar{P}_s \bar{h} \bar{P}_s + \bar{\eta}^{\dagger}\, \bar{g}_{\perp}(z)\, \bar{\eta}, \tag{16}$$

where $\bar{g}_{\perp}(z) = (\hbar z - \bar{Q}_p \bar{h} \bar{Q}_p)^{-1}$, $\bar{\eta} = \bar{Q}_p \bar{h} \bar{P}_s$, $\bar{h}$ is the matrix of the s-p Hamiltonian in Eq. (3), and $\bar{P}_s$ and $\bar{Q}_p$ are the projection operators for s-orbital and p-orbital bases, respectively. The effective Hamiltonian is thereby decomposed into three parts as follows:

$$H_{\rm eff}(z) = H^{ss\sigma}_{\rm hop} + H^{\rm 2nd}_{\rm hop}(z) + H^{\rm eff}_{\rm SOI}(z). \tag{17}$$

The first term $H^{ss\sigma}_{\rm hop}$ represents the nearest-neighbor hopping between s orbitals in Eq. (4). The second term $H^{\rm 2nd}_{\rm hop}(z)$ represents the second-nearest-neighbor hopping through the s-p hybridization, which is given by

$$H^{\rm 2nd}_{\rm hop}(z) = \sum_{\boldsymbol{R},\boldsymbol{\delta}^{\rm i}\boldsymbol{\delta}^{\rm o}} \sum_{\sigma} \varepsilon_{\boldsymbol{\delta}^{\rm i}\boldsymbol{\delta}^{\rm o}}\, \varphi^{\dagger}_{s\sigma}(\boldsymbol{R} + a\boldsymbol{\delta}^{\rm o})\varphi_{s\sigma}(\boldsymbol{R} - a\boldsymbol{\delta}^{\rm i}), \tag{18}$$

where

$$\varepsilon_{\boldsymbol{\delta}^{\rm i}\boldsymbol{\delta}^{\rm o}} = -u(z)\,(\boldsymbol{\delta}^{\rm i} \cdot \boldsymbol{\delta}^{\rm o}), \tag{19a}$$

$$u(z) = \frac{-t^2_{sp\sigma}(\hbar z - \Delta_p + \lambda)}{(\hbar z - \Delta_p - \lambda)(\hbar z - \Delta_p + 2\lambda)}, \tag{19b}$$

and $\boldsymbol{\delta}^{\rm i}$ and $\boldsymbol{\delta}^{\rm o}$ are the direction cosines to the nearest-neighbor sites of $\boldsymbol{R}$.

The third term $H^{\rm eff}_{\rm SOI}(z)$ represents the effective spin-orbit interaction, which is also induced by the s-p hybridization as

$$H^{\rm eff}_{\rm SOI}(z) = \frac{2\alpha(z)}{\hbar^2} \sum_{\boldsymbol{R},\boldsymbol{\delta}^{\rm i}\boldsymbol{\delta}^{\rm o}} \sum_{\sigma\sigma'} \boldsymbol{l}_{\boldsymbol{\delta}^{\rm i}\boldsymbol{\delta}^{\rm o}} \cdot \boldsymbol{s}_{\sigma\sigma'}\, \varphi^{\dagger}_{s\sigma}(\boldsymbol{R} + a\boldsymbol{\delta}^{\rm o})\varphi_{s\sigma'}(\boldsymbol{R} - a\boldsymbol{\delta}^{\rm i}), \tag{20}$$

where

$$\boldsymbol{l}_{\boldsymbol{\delta}^{\rm i}\boldsymbol{\delta}^{\rm o}} = i\hbar(\boldsymbol{\delta}^{\rm i} \times \boldsymbol{\delta}^{\rm o}), \tag{21a}$$

$$\alpha(z) = \frac{t^2_{sp\sigma}\lambda}{(\hbar z - \Delta_p - \lambda)(\hbar z - \Delta_p + 2\lambda)}. \tag{21b}$$

Effective spin-orbit interaction $H_{\rm SOI}^{\rm eff}$ arises from the coupling between the orbital angular momentum generated by two successive $sp\sigma$ hoppings and the on-site atomic spin-orbit coupling in the absence of local spatial-inversion symmetry with nonzero $\boldsymbol{\delta}^{\rm i} \times \boldsymbol{\delta}^{\rm o}$. Reflecting this, in our effective model, $\boldsymbol{l}_{\boldsymbol{\delta}^{\rm i}\boldsymbol{\delta}^{\rm o}}$ takes a finite value only at the V-shaped edge at $n = 0$ within the nearest-neighbor $sp\sigma$ hopping:

$$l^z_{\boldsymbol{\delta}^{\rm i}\boldsymbol{\delta}^{\rm o}} = \begin{cases} \pm i\hbar \sin\theta & (\boldsymbol{\delta}^{\rm i} = \boldsymbol{R}_0 - \boldsymbol{R}_{\mp 1}, \quad \boldsymbol{\delta}^{\rm o} = \boldsymbol{R}_{\pm 1} - \boldsymbol{R}_0), \\ 0 & (\text{otherwise}). \end{cases} \tag{22}$$

From the symmetry viewpoint, the imaginary hopping $i(\boldsymbol{\delta}^{\rm i} + \boldsymbol{\delta}^{\rm o})$ can be interpreted as the activation of the magnetic toroidal dipole $\boldsymbol{T}$ corresponding to a time-reversal-odd polar vector, while the spin degree of freedom $\bar{s}$ can be regarded as the magnetic dipole $\boldsymbol{M}$ corresponding to a time-reversal-odd axial vector [22,24]. Consequently, $H_{\rm SOI}^{\rm eff}$ incorporates the symmetry of the electric dipole $\boldsymbol{Q}$ ($\sim \boldsymbol{T} \times \boldsymbol{M}$) corresponding to a time-reversal-even polar vector, thereby encoding the polarity associated with the geometric shape. Specifically, $\boldsymbol{T}$, $\boldsymbol{M}$, and $\boldsymbol{Q}$ are induced in the x, z, and y directions, respectively, in the present setup.

To calculate the ME tensor using the effective Hamiltonian as Eq. (17), we introduce an effective ME tensor:

$$\alpha_{\rm eff}^{\nu;\rho} = \alpha_{\rm eff}^{\nu;\rho}(i\omega_m)\big|_{i\omega_m \to 0+i\gamma}. \tag{23}$$

The effective ME tensor defined in terms of the bosonic Matsubara frequencies $\omega_m = 2m\pi k_{\rm B}T/\hbar$ is expressed by [71,72]

$$\alpha_{\rm eff}^{\nu;\rho}(i\omega_m) = -\frac{k_{\rm B}T}{V} \sum_{i\epsilon_n} {\rm Tr}\big[\bar{M}^{\nu}_{\rm eff}\bar{\mathcal{G}}_{\rm eff}(i\epsilon_n + i\omega_m)\bar{P}^{\rho}\bar{\mathcal{G}}_{\rm eff}(i\epsilon_n)\big], \tag{24}$$

where $\epsilon_n = (2n+1)\pi k_{\rm B}T/\hbar$ is the fermionic Matsubara frequencies and $\bar{P}^{\rho}$ is the matrix of polarization operator defined in Eq. (13). $\bar{\mathcal{G}}_{\rm eff}(z)$ is the Green's function of the effective Hamiltonian (the effective Green's function), which is defined as follows:

$$\bar{\mathcal{G}}_{\rm eff}(z) = \frac{1}{\hbar z + \mu - \bar{h}_{\rm eff}(z + \mu/\hbar)}, \tag{25}$$

where μ is the chemical potential. The effective Green's function represents the result of incorporating the p-orbital contribution into the s-orbital Green's function through the s-p hybridization [70]:

$$\bar{\mathcal{G}}_{\rm eff}(z - \mu/\hbar) = \bar{g}_{\parallel}(z) + \bar{g}_{\parallel}(z)\bar{\eta}^{\dagger}\bar{g}_{\perp}(z)\bar{\eta}\bar{g}_{\parallel}(z) + \cdots, \tag{26}$$

where $\bar{g}_{\parallel}(z) = (\hbar z - \bar{P}_s\bar{h}\bar{P}_s)^{-1}$. In order to take into account the contribution of orbital magnetization originating only from the p-orbital basis, we introduce an effective magnetization operator $\bar{M}^{\nu}_{\rm eff} = \bar{M}^{\nu}_{\rm eff}(i\epsilon_n, i\epsilon_n + i\omega_m)$,

$$\bar{M}^{\nu}_{\rm eff}(z_1, z_2) = \bar{P}_s\bar{M}^{\nu}\bar{P}_s + \bar{\eta}^{\dagger}\bar{g}_{\perp}(z_1 + \mu/\hbar)\bar{M}^{\nu}\bar{g}_{\perp}(z_2 + \mu/\hbar)\bar{\eta}. \tag{27}$$

The effective Green's function in Eq. (25), the effective magnetization operator in Eq. (27), and the effective ME tensor in Eq. (24) are illustrated by the Feynman diagrams shown in Figs. 3(a)–3(c), respectively. For the bubble diagram confined within the s-orbital subspace, the effects of the s-p hybridization and the magnetic elements defined on the p orbitals are incorporated. As shown in Eq. (26) and Fig. 3(a), by including the s-p hybridization in the Green's function to infinite order with even numbers of hybridization processes, the effective Green's function $\bar{\mathcal{G}}_{\rm eff}$ is obtained. The Green's function components containing an odd number of s-p hybridizations propagate through another Green's function, which also includes an odd number of hybridizations mediated by the magnetic operator defined on the p orbitals. Consequently, the effective ME tensor defined in Eq. (24) emerges.

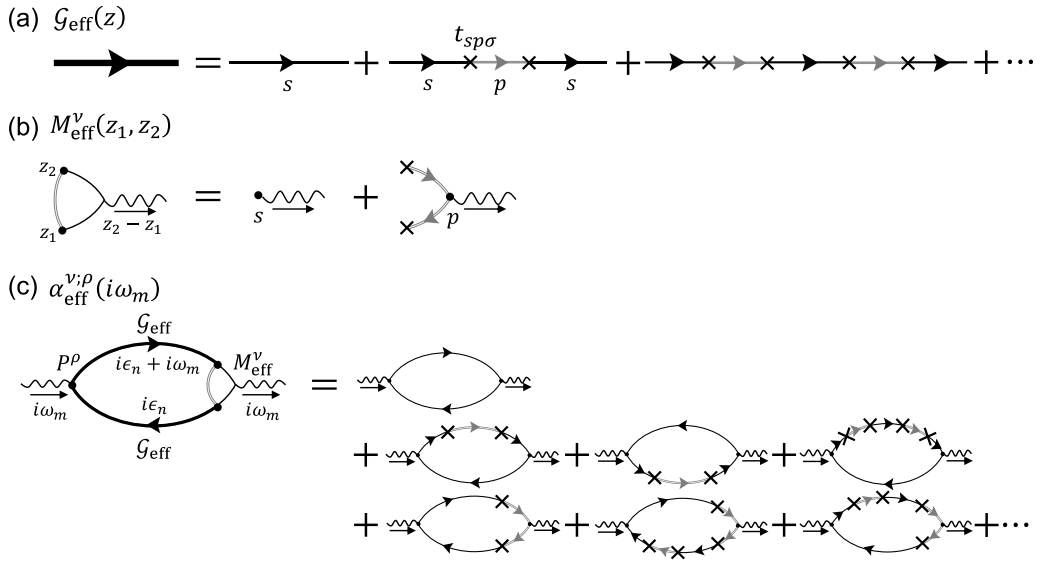


FIG. 3. (a) Diagrams representing the effective Green's function in Eq. (25). The thick black line represents the effective Green's function $\bar{\mathcal{G}}_{\rm eff}$ in Eq. (25), the thin black line denotes the Green's function propagating between s orbitals $\bar{g}_{\parallel}$, and the gray double line represents the Green's function propagating between p orbitals $\bar{g}_{\perp}$. The cross symbol ($\times$) indicates the s-p orbital hybridization $\bar{\eta}$. As shown in Eq. (26), the effective Green's function represents the result of incorporating the p-orbital effect into the s-orbital Green's function through the s-p hybridization. (b) Diagrams representing the effective magnetization operator in Eq. (27). The vertex accompanied by a wavy line represents the magnetization operator $\bar{M}^{\nu}$. (c) Diagrams representing the effective ME tensor in Eq. (24). The p-orbital contribution is included via the s-p hybridization in the bubble diagram closed within the s orbitals.

IV. SHAPE-INDUCED EFFECTS IN THE GREEN'S FUNCTION

We evaluate the angular dependence of the Green's function in Eq. (25). The Hamiltonian matrix can be separated into the $\theta = \pi$ component and the remaining contributions as follows:

$$\bar{h}_{\rm eff} = \bar{h}_{\rm eff}\big|_{\theta=\pi} + \Delta\bar{h}^{(\theta)}_{\rm eff}. \tag{28}$$

In our effective model in Eq. (17), $\Delta\bar{h}^{(\theta)}_{\rm eff}$ takes a finite value only on the sites adjacent to the apex of the V-shaped 1D chain, as shown in Eq. (22). Therefore, $\Delta\bar{h}^{(\theta)}_{\rm eff}$ is given by 4×4 matrix:

$$\Delta\bar{h}^{(\theta)}_{\rm eff}(z) = \begin{pmatrix} 0, & u(z)(1+\cos\theta)\bar{\sigma}_0 - i\alpha(z)\sin\theta\bar{\sigma}_z \\ (-i \to i), & 0 \end{pmatrix}, \tag{29}$$

where the matrix representation corresponds to the two sites adjacent to the apex angle of the V-shaped 1D chain, $\boldsymbol{R}_{-1}$ and $\boldsymbol{R}_{+1}$, in Eq. (2). $\bar{\sigma}_0$ and $\bar{\sigma}_{\nu}$ ($\nu = x, y, z$) are the identity matrix and Pauli matrices for spin, respectively. In this section, $(-i \to i)$ denotes taking the conjugate transpose without taking the conjugate of the coefficients [e.g., $u(z)$ and $\alpha(z)$]. Here, it corresponds to the other off-diagonal component obtained by replacing $-i$ with i.

Then, using $\Delta\bar{h}^{(\theta)}_{\rm eff}$, the following Dyson equation is obtained:

$$\bar{\mathcal{G}}_{\rm eff} = \bar{\mathcal{G}}^{(\pi)}_{\rm eff} + \bar{\mathcal{G}}^{(\pi)}_{\rm eff}\Delta\bar{h}^{(\theta)}_{\rm eff}\bar{\mathcal{G}}_{\rm eff}, \tag{30}$$

where $\bar{\mathcal{G}}^{(\pi)}_{\rm eff} = \bar{\mathcal{G}}_{\rm eff}|_{\theta=\pi}$. It is noted that when $\theta = \pi$, the V-shaped 1D chain represented by Eq. (2) corresponds to a simple 1D chain with the spatial-inversion symmetry. Accordingly, $\bar{\mathcal{G}}^{(\pi)}_{\rm eff}$ is evaluated analytically, with the detailed derivation presented in Appendix A. Then, by solving Eq. (30),

we obtain the following expression:

$$\bar{\mathcal{G}}_{\rm eff} = \bar{\mathcal{G}}^{(\pi)}_{\rm eff} + \bar{\mathcal{G}}^{(\pi)}_{\rm eff}\,\bar{\mathcal{T}}^{(\theta)}\,\bar{\mathcal{G}}^{(\pi)}_{\rm eff}, \tag{31}$$

where $\bar{\mathcal{T}}^{(\theta)}$ is the transition matrix (T-matrix) with respect to the V-shaped geometry:

$$\bar{\mathcal{T}}^{(\theta)}(z) = \Delta\bar{h}^{(\theta)}_{\rm eff}\frac{1}{1-\bar{\mathcal{G}}^{(\pi)}_{\rm eff}\,\Delta\bar{h}^{(\theta)}_{\rm eff}}. \tag{32}$$

The deviation from the straight chain is localized around the apex at $n = 0$. Consequently, the effect of the V-shaped geometry can be represented in a form analogous to the T-matrix formalism for a local perturbation, in close analogy to impurity scattering [73,74]. Therefore, the T-matrix $\bar{\mathcal{T}}^{(\theta)}$ encodes information about the shape of the Hamiltonian. Moreover, since the T-matrix reflects the local effects of the shape, it can be analyzed within a smaller subspace than the full Hamiltonian, expressed as the $2(2N+1)\times 2(2N+1)$ matrix. In our effective model in Eq. (17), $\bar{\mathcal{T}}^{(\theta)}$ is given by the following 4×4 matrix:

$$\bar{\mathcal{T}}^{(\theta)}(z) = \begin{pmatrix} \mathcal{T}_{q^{\rm c}_0\sigma_0}\bar{\sigma}_0, & \mathcal{T}_{q^{\rm b}_0\sigma_0}\bar{\sigma}_0 - i\mathcal{T}_{t^{\rm b}_x\sigma_z}\bar{\sigma}_z \\ (-i\to i), & \mathcal{T}_{q^{\rm c}_0\sigma_0}\bar{\sigma}_0 \end{pmatrix}. \tag{33}$$

$\mathcal{T}_{q^{\rm c}_0\sigma_0}$, $\mathcal{T}_{q^{\rm b}_0\sigma_0}$, and $\mathcal{T}_{t^{\rm b}_x\sigma_z}$ are nonzero components in $\bar{\mathcal{T}}^{(\theta)}$. To characterize the symmetry properties of the geometry-induced scattering processes, we decompose the T-matrix into multipole components, whose coefficients are indicated by the subscripts: $q^{\rm c}_0$, $q^{\rm b}_0$, and $t^{\rm b}_x$ denote the multipoles defined in the two-site subspace, which will be introduced later in Sec. V and Appendix C. Nonzero off-diagonal components over two sites in $\bar{\mathcal{T}}^{(\theta)}$ are mainly determined by $\Delta\bar{h}^{(\theta)}_{\rm eff}$, which is composed of the second-nearest-neighbor hopping ($\sim q^{\rm b}_0\sigma_0$) and the effective spin-orbit interaction (product of imaginary hopping and spin $\sim t^{\rm b}_x\sigma_z$), as shown in Eq. (29). In contrast, the diagonal components are mainly determined by $(\Delta\bar{h}^{(\theta)}_{\rm eff})^2$ ($\sim q^{\rm c}_0\sigma_0$).

Similarly to the Hamiltonian matrix in Eq. (28), the angular θ dependence of the effective magnetization is separated as follows:

$$\bar{M}^{\nu}_{\rm eff} = \bar{M}^{\nu(\pi)}_{\rm eff} + \Delta\bar{M}^{\nu(\theta)}_{\rm eff}, \tag{34}$$

where $\bar{M}^{\nu(\pi)}_{\rm eff} = \bar{M}^{\nu}_{\rm eff}|_{\theta=\pi}$. In our effective model in Eq. (17), $\Delta\bar{M}^{z(\theta)}_{\rm eff}$ is, like $\bar{\mathcal{T}}^{(\theta)}$, given by the 4×4 matrix as follows:

$$\Delta\bar{M}^{z(\theta)}_{\rm eff}(z_1,z_2) = \begin{pmatrix} 0, & \Delta M_{q^{\rm b}_0\sigma_z}\bar{\sigma}_z - i\Delta M_{t^{\rm b}_x\sigma_0}\bar{\sigma}_0 \\ (-i\to i), & 0 \end{pmatrix}, \tag{35}$$

where $\Delta M_{q^{\rm b}_0\sigma_z}$ and $\Delta M_{t^{\rm b}_x\sigma_0}$ are nonzero components in $\Delta\bar{M}^{z(\theta)}_{\rm eff}$; $\Delta M_{q^{\rm b}_0\sigma_z}$ corresponds to the contribution from the spin magnetization, while $\Delta M_{t^{\rm b}_x\sigma_0}$ corresponds to that from the orbital magnetization. In our model, $\Delta\bar{M}^{z(\theta)}_{\rm eff}$ is constrained to the form given in Eq. (35) through Eq. (27), analogous to $\Delta\bar{h}^{(\theta)}_{\rm eff}$ [Eq. (29)].

We evaluate the apex angle θ dependence of $\bar{\mathcal{T}}^{(\theta)}$ and $\Delta\bar{M}^{z(\theta)}_{\rm eff}$. We set the Hamiltonian parameters given in Eq. (14). We also set the chemical potential $\mu = 0.5$ and the complex frequencies that are arguments of $\bar{\mathcal{T}}^{(\theta)}$ and $\Delta\bar{M}^{z(\theta)}_{\rm eff}$: $z = z_1 = z_2 = 0.5\pi i$. Figure 4(a) shows θ dependences of $\bar{\mathcal{T}}^{(\theta)}$, where we find that each coefficient is expressed by the following expressions as

$$\mathcal{T}_{q^{\rm c}_0\sigma_0} \propto \Delta_p^{-2}(1+\cos\theta)^2, \quad \mathcal{T}_{q^{\rm b}_0\sigma_0} \propto \Delta_p^{-1}(1+\cos\theta), \quad \mathcal{T}_{t^{\rm b}_x\sigma_z} \propto \Delta_p^{-2}\sin\theta. \tag{36}$$

This dependence is obtained by analyzing the following expression:

$$\bar{\mathcal{T}}^{(\theta)}(z) = \Delta\bar{h}^{(\theta)}_{\rm eff} + O\big(\Delta\bar{h}^{(\theta)}_{\rm eff}\bar{\mathcal{G}}^{(\pi)}_{\rm eff}\Delta\bar{h}^{(\theta)}_{\rm eff}\big) \quad (\Delta_p\to\infty). \tag{37}$$

Compared to Eq. (29), the off-diagonal components $\mathcal{T}_{q^{\rm b}_0\sigma_0}$ and $\mathcal{T}_{t^{\rm b}_x\sigma_z}$ reflect the Δ_p and θ dependence of the second-nearest-neighbor hopping ($u\propto\Delta_p^{-1}$) and the effective spin-orbit interaction

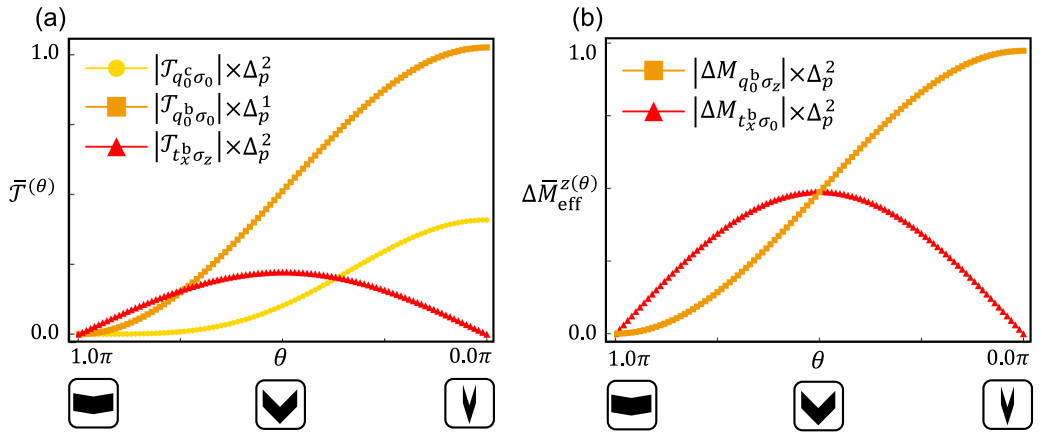


FIG. 4. Absolute values of the components of (a) $\bar{\mathcal{T}}^{(\theta)}$ and (b) $\Delta\bar{M}_{\rm eff}^{z(\theta)}$ as a function of the apex angle θ. We fix the chemical potential $\mu = 0.5$ and the complex frequencies $z = z_1 = z_2 = 0.5\pi i$, and we use the other model parameters in Eq. (14) and $N = 128$. In both cases, the terms including $q_0^{\rm c}$ and $q_0^{\rm b}$ exhibit a $(1+\cos\theta)$-type behavior, whereas that including $t_x^{\rm b}$ shows a $\sin\theta$-type dependence. Furthermore, the obtained results display the Δ_p dependence consistent with Eqs. (27) and (37).

($\alpha \propto \Delta_p^{-2}$), respectively. Moreover, the diagonal component $\mathcal{T}_{q_0^{\rm c}\sigma_0}$ arises through the square of the second-nearest-neighbor hopping at the lowest order in Δ_p^{-1}. It is also noted from the above equation in Eq. (37) that when $\bar{\mathcal{G}}_{\rm eff}^{(\pi)}(z)$ becomes large (e.g., when Imz is sufficiently small and Rez corresponds to the resonant frequency), this power expansion breaks down, and the θ dependence deviates from Eq. (36).

In the same manner, the θ dependence of $\Delta\bar{M}_{\rm eff}^{z(\theta)}$ in Fig. 4(b) is given as follows:

$$\Delta M_{q_0^{\rm b}\sigma_z} \propto \Delta_p^{-2}(1+\cos\theta), \quad \Delta M_{t_x^{\rm b}\sigma_0} \propto \Delta_p^{-2}\sin\theta. \tag{38}$$

This behavior is understood from Eq. (27); $\bar{g}_\perp(z) \propto \Delta_p^{-1}(\Delta_p \gg z)$ at the lowest order in Δ_p^{-1}. $\Delta M_{q_0^{\rm b}\sigma_z}$ and $\Delta M_{t_x^{\rm b}\sigma_0}$ arise from the even- and odd-order terms of the angular momentum operator $\bar{l}^z$, as given in Eqs. (19) and (21), respectively. Therefore, the resulting θ dependence is analogous to that of $\Delta\bar{h}_{\rm eff}^{(\theta)}$ shown in Eq. (29). Furthermore, because the angular dependence originates solely from $\bar{\eta}$, no θ dependence appears in the denominator term; consequently, Eq. (38) appears as a direct proportional relation, unlike $\bar{\mathcal{T}}^{(\theta)}$.

V. MULTIPOLE-BASED SELECTION RULES

Finally, we introduce the multipole basis and clarify the underlying mechanism by taking into account the selection rules. By employing the symmetry-adapted multipole basis [22–26,75–77], arbitrary operators such as the effective Hamiltonian can be expanded by the products of the cluster and bond degrees of freedom (denoted as cluster multipole and bond multipole, respectively) and the spin degree of freedom.

Table I summarizes the multipole degrees of freedom included in each operator in our effective model. The on-site degrees of freedom are described by the cluster electric multipole $\bar{q}^{\rm c}$, while the off-site degrees of freedom are described by the bond electric multipole $\bar{q}^{{\rm b}n}$ and the bond magnetic toroidal multipole $\bar{t}^{{\rm b}n}$; the former (latter) corresponds to the real (imaginary) hopping. Here, the superscript n denotes the bond between the nth nearest-neighbor sites, and the prime ($'$) indicates the quantity defined only on the two sites adjacent to the apex angle ($\boldsymbol{R}_{-1}$ and $\boldsymbol{R}_{+1}$) of the V-shaped 1D chain. The spin degrees of freedom are represented by the Pauli matrices: $\bar{\sigma}_0$ corresponds to the

TABLE I. List of multipoles included in the representative operators related to the ME tensor. For simplicity, notations such as "–" are omitted (e.g., $\mathcal{G}^{(\pi)} = \bar{\mathcal{G}}^{(\pi)}_{\rm eff}$). In the multipole notation, the superscripts c and b denote cluster and bond multipoles, the superscript n following b denotes the nth nearest neighbor, the subscripts 0 and (x, y) denote the monopole and dipole, respectively, and the prime ($'$) indicates the quantity defined on the two sites adjacent to the apex angle ($\boldsymbol{R}_{-1}$ and $\boldsymbol{R}_{+1}$) of the V-shaped 1D chain. For $\bar{M}^{z(\pi)}_{\rm eff}$, the edge correction due to the second-nearest-neighbor hopping to the on-site term is not taken into account. In the second column, the corresponding irreducible representations under the point group C_{2v} are shown, where the superscript $\pm$ denotes the parity with respect to the time-reversal operation. In the last column, the dependence on the apex angle θ and the s-p energy separation Δ_p ($\Delta_p \to \infty$) is shown.

Operator	Irreducible representation	Relevant multipole	θ, Δ_p dependence
$\mathcal{G}^{(\pi)}$	A_1^+	$q_0^{\rm c}\sigma_0,\ q_0^{\rm b1}\sigma_0,\ q_0^{\rm b2}\sigma_0, \ldots$	$\propto 1$
$M^{z(\pi)}$	B_1^-	$q_0^{\rm c}\sigma_z$	$\propto 1$
		$q_0^{\rm b2}\sigma_z$	$\propto \Delta_p^{-2}$
$\mathcal{T}^{(\theta)}$	A_1^+	$q_0^{\rm c\prime}\sigma_0$	$\sim \Delta_p^{-2}(1+\cos\theta)^2$
		$q_0^{\rm b2\prime}\sigma_0$	$\sim \Delta_p^{-1}(1+\cos\theta)$
		$t_x^{\rm b2\prime}\sigma_z$	$\sim \Delta_p^{-2}\sin\theta$
$\Delta M^{z(\theta)}$	B_1^-	$q_0^{\rm b2\prime}\sigma_z$	$\propto \Delta_p^{-2}(1+\cos\theta)$
		$t_x^{\rm b2\prime}\sigma_0$	$\propto \Delta_p^{-2}\sin\theta$
P^x	B_1^+	$q_x^{\rm c}\sigma_0$	$\propto \sin\theta/2$
P^y	A_1^+	$q_y^{\rm c}\sigma_0$	$\propto \cos\theta/2$

electric monopole, while $(\bar{\sigma}_x,\ \bar{\sigma}_y,\ \bar{\sigma}_z)$ represents the magnetic dipole. The matrix representations of the relevant multipoles are given in Appendix B.

Table I presents the dependence on the apex angle θ and the s-p energy separation Δ_p for $\Delta_p \to \infty$. The simple 1D chain Green's function $\bar{\mathcal{G}}^{(\pi)}_{\rm eff}$ includes all cluster and bond multipoles generated by arbitrary powers of the hopping Hamiltonian. The simple 1D chain effective magnetization $\bar{M}^{z(\pi)}_{\rm eff}$ contains $\bar{q}_0^{\rm c}\bar{\sigma}_z$ component and also has $\bar{q}_0^{\rm b2}\bar{\sigma}_z$ component associated with the second-nearest-neighbor hopping. Both originate from the spin magnetization contribution. $\bar{\mathcal{T}}^{(\theta)}$ and $\Delta\bar{M}^{z(\theta)}_{\rm eff}$ are discussed in Sec. IV. It is noteworthy that, once the effective magnetization is introduced, the magnetic dipole operator is no longer a pure magnetic dipole but acquires an admixture of the magnetic toroidal dipole $\bar{t}_x^{\rm b2\prime}\bar{\sigma}_0$. Although the magnetic dipole and the magnetic toroidal dipole are distinct multipoles, they belong to the same irreducible representation in the present system. The multipole $\bar{t}_x^{\rm b2\prime}\bar{\sigma}_0$ arises from the coupling between the orbital magnetization and the $sp\sigma$ hopping. Finally, the θ dependence of $\bar{P}^x$ and $\bar{P}^y$ is given from Eq. (2).

In order for the ME tensor defined in Eq. (24) to acquire a finite value, the condition $\mathrm{Tr}[*] \neq 0$ must be satisfied. Within the framework of the multipole basis, the following relations play a key role:

$$\bar{q}_0^{\rm b2\prime}\,\bar{t}_x^{\rm b2\prime}\,\bar{q}_x^{\rm c} = -i\,\bar{q}_0^{\rm c\prime}, \tag{39a}$$

$$\bar{\sigma}_z\,\bar{\sigma}_z = \bar{\sigma}_0. \tag{39b}$$

From the symmetry viewpoint, these equations represent $A_1^+ \otimes B_1^- \otimes B_1^+ = A_1^-$ and $B_1^- \otimes B_1^- = A_1^+$, respectively. By taking into account the above processes and extracting the contributions that satisfy Eq. (39) while retaining only the terms in powers of Δ_p^{-1}, the dominant contributions can be expressed as

$$\alpha^{z;x}_{\rm eff}(i\omega_m) = \alpha^{z;x}_{\rm i} + \alpha^{z;x}_{\rm ii} + \alpha^{z;x}_{\rm iii} + \alpha^{z;x}_{\rm iv} + O\big(\Delta_p^{-4}\big). \tag{40}$$

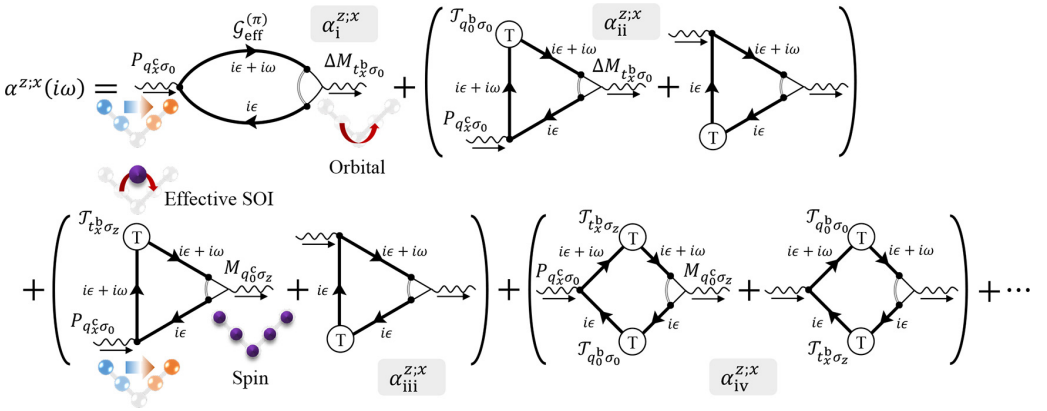


FIG. 5. Diagrams representing distinct processes for the ME effect in our effective models. The thick black line represents the simple 1D chain Green's function at $\theta = \pi$, and the circled T (Ⓣ) represents the T-matrix about the V shape in Eq. (32). The subscripts of the Matsubara frequencies are omitted. The symbols (e.g., $P_{q_x^{\rm c}\sigma_0}$) attached to the operators correspond to their multipole components in Table I. The physical mechanisms corresponding to each multipole component are shown along with their schematic illustrations (see also Fig. 8 in Appendix B). There are two primary physical mechanisms contributing to the ME effect: One is the coupling between the charge-potential gradient induced by the incident electric field and the orbital magnetization ($\alpha_{\rm i}^{z;x}$ and $\alpha_{\rm ii}^{z;x}$). The other is the spin magnetizations induced by the electric field through the effective spin-orbit interaction ($\alpha_{\rm iii}^{z;x}$ and $\alpha_{\rm iv}^{z;x}$).

The corresponding diagrams are schematically shown in Fig. 5. The detailed calculations and the explicit expressions are provided in Appendix C. From Table I, the θ and Δ_p dependence of $\alpha_{\rm i}^{z;x}$, $\alpha_{\rm ii}^{z;x}$, $\alpha_{\rm iii}^{z;x}$, and $\alpha_{\rm iv}^{z;x}$ is given as follows:

$$\alpha_{\rm i}^{z;x} \propto \Delta_p^{-2} \sin\theta \sin\frac{\theta}{2}, \tag{41a}$$

$$\alpha_{\rm ii}^{z;x} \sim \Delta_p^{-3}(1+\cos\theta)\sin\theta \sin\frac{\theta}{2}, \tag{41b}$$

$$\alpha_{\rm iii}^{z;x} \sim \Delta_p^{-2} \sin\theta \sin\frac{\theta}{2}, \tag{41c}$$

$$\alpha_{\rm iv}^{z;x} \sim \Delta_p^{-3}(1+\cos\theta)\sin\theta \sin\frac{\theta}{2}. \tag{41d}$$

As illustrated in Fig. 5, the ME response in our model arises from two distinct processes. The components $\alpha_{\rm i}^{z;x}$ and $\alpha_{\rm ii}^{z;x}$ are represented by the coupling among the polarization ($P_{q_x^{\rm c}\sigma_0}$) and the magnetization ($\Delta M_{t_x^{\rm b}\sigma_0}$) through the hopping across the apex angle ($\bar{q}_0^{\rm b2}\bar{\sigma}_0$) in the Green's function, where $P_{q_x^{\rm c}\sigma_0}$ and $\Delta M_{t_x^{\rm b}\sigma_0}$ represent the charge-potential gradient induced by the applied electric field and the orbital magnetization, respectively. Thus, $\alpha_{\rm i}^{z;x}$ ($\alpha_{\rm ii}^{z;x}$) represents the (higher-order) contributions arising from the coupling between charge-potential gradient and the orbital magnetization. In contrast, the components $\alpha_{\rm iii}^{z;x}$ and $\alpha_{\rm iv}^{z;x}$ are represented by the coupling among the polarization ($P_{q_x^{\rm c}\sigma_0}$), the spin magnetization ($M_{q_0^{\rm c}\sigma_z}$), and the spin-dependent hopping across the apex angle in the T-matrix ($\bar{t}_x^{\rm b2\prime}\bar{\sigma}_z$). Since $\bar{t}_x^{\rm b2\prime}\bar{\sigma}_z$ represents the contribution from the effective spin-orbit interaction [Eq. (37)], $\alpha_{\rm iii}^{z;x}$ ($\alpha_{\rm iv}^{z;x}$) is interpreted as the (higher-order) couplings between the charge-potential gradient and spin magnetizations via the effective spin-orbit interaction.

Figure 6 shows the θ dependence of the components $\alpha_{\rm i}^{z;x}$, $\alpha_{\rm ii}^{z;x}$, $\alpha_{\rm iii}^{z;x}$, and $\alpha_{\rm iv}^{z;x}$ at the chemical potential $\mu = 0.5$, where we use the same model parameters as those in Fig. 2(a). For the analytic continuation from $i\omega_m$ to $0 + i\gamma$, we employed the barycentric rational function approximation method [78]. Here, the fermionic Matsubara frequencies were summed from $n = -100$ to 100,

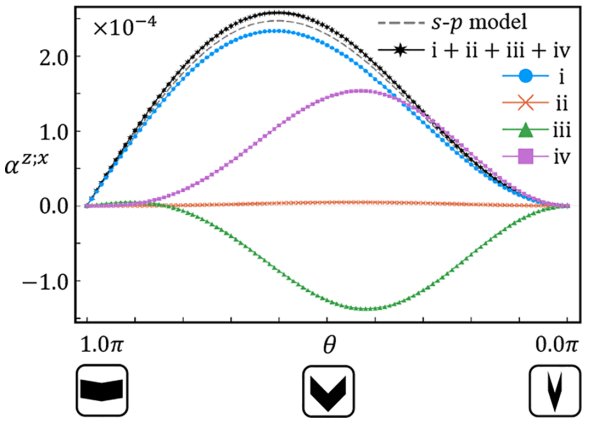


FIG. 6. Apex angle θ dependence of the components of the effective ME tensor $\alpha_{\rm i}^{z;x}$, $\alpha_{\rm ii}^{z;x}$, $\alpha_{\rm iii}^{z;x}$, and $\alpha_{\rm iv}^{z;x}$. We also present their total contribution and the result calculated using the Kubo formula [Eq. (9)] in the s-p model. We use the same model parameters as those in Fig. 2(a). For the analytic continuation, we employed the barycentric rational function approximation method [78].

while the bosonic Matsubara frequency data were taken over the range $m = 0$ to 30. We also present their total contribution and the result calculated by using the Kubo formula [Eq. (9)] in the original s-p model. It is demonstrated that the summation of the above four components successfully reproduces the result obtained from the s-p model, indicating the dominant contributions are given by $\alpha_{\rm i}^{z;x}$–$\alpha_{\rm iv}^{z;x}$. Among them, we find that the contribution from $\alpha_{\rm i}^{z;x}$ is the most dominant, and thereby, the θ dependence of the total $\alpha_{\rm eff}^{z;x}$ is governed as

$$\alpha_{\rm eff}^{z;x} \propto \sin\theta \sin\frac{\theta}{2}. \tag{42}$$

This behavior arises from the competition between the maximization of the orbital angular momentum at the angle of the V shape ($\propto \sin\theta$) and the gain in the charge-potential gradient induced by the electric field along the x direction ($\propto \sin\theta/2$). It exhibits a peak at $\theta = 2\tan^{-1}\sqrt{2} \approx 0.608\pi$, which is consistent with the result in Fig. 2(b).

VI. FERROMAGNETIC SYSTEM

In this section, we consider the effect of the time-reversal-symmetry breaking by additionally taking into account the ferromagnetic mean field along the z direction. For that purpose, we include a Zeeman interaction in the Hamiltonian:

$$H_{\rm Zee} = \frac{b}{\hbar}(L^z + {\rm g}S^z). \tag{43}$$

The introduction of a ferromagnetic moment along the z direction induces a magnetic toroidal dipole T_x along the x direction through its coupling to the electric polarization along the y direction, which arises from the V-shaped geometry. Consequently, from the viewpoint of symmetry, the ME response driven by the magnetic toroidal dipole, i.e., the magnetic-driven ME, is induced in the $\alpha^{z;y}$ component [19,21,24].

We investigate the shape dependence of the isothermal ME tensor $\alpha_{\rm T}^{z;y} = \alpha^{z;y}|_{\gamma=0}$ in the V-shaped s-p model. Figure 7(a) shows the θ dependence of the isothermal ME response. We use the Hamiltonian parameters in Eq. (14) and $b = 0.3$; the other parameters are set to $N = 128$, $\mu = 2$, and $T = 0.01$. In contrast to the previous results of nonmagnetic-driven $\alpha^{z;x}$, the magnitude increases monotonically as the apex angle θ decreases.

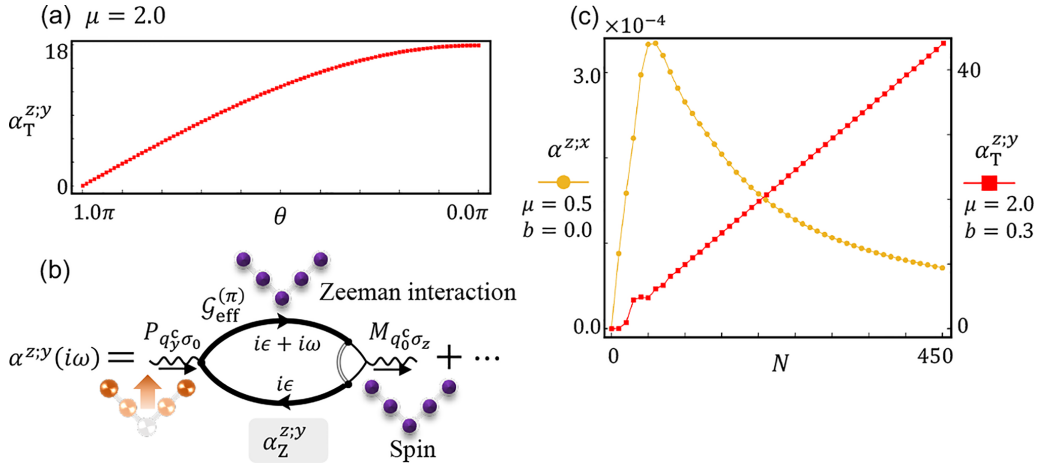


FIG. 7. (a) Apex angle θ dependence of the isothermal ME tensor $\alpha_{\rm T}^{z;y}$ at $\mu = 2$ in the ferromagnetic s-p model. We set the Hamiltonian parameters as Eq. (14), and $N = 128$ and $T = 0.01$. The ME response increases monotonically as the apex angle θ decreases. (b) Diagrams for the ME effect in the ferromagnetic V-shaped model. (c) The V-shaped lattice size N dependence of the nonmagnetic-driven ME tensor $\alpha^{z;x}$ ($\mu = 0.5,\ b = 0$) and the magnetic-driven ME tensor $\alpha_{\rm T}^{z;y}$ ($\mu = 2,\ b = 0.3$) at $\theta = \pi/2$. The difference in physical mechanisms results in different size dependence.

In the magnetic-driven ME response, the underlying mechanism is more straightforward than that of the nonmagnetic-driven $\alpha^{z;x}$, since the Zeeman interaction introduces an additional component into $\bar{\mathcal{G}}^{(\pi)}$ as $\bar{q}_0^c\bar{\sigma}_z$, which leads to a natural expansion as follows:

$$\alpha_{\rm eff}^{z;y}(i\omega_m) = \alpha_{\rm Z}^{z;y} + O\left(\Delta_p^{-1}\right). \tag{44}$$

$\alpha_{\rm T}^{z;y}$ and $\alpha_{\rm eff}^{z;y}(i\omega_m)$ are related by Eq. (23). The corresponding diagram is shown in Fig. 7(b), and its explicit expressions are provided in Appendix C. The diagram in Fig. 7(b) displays that $\alpha_{\rm T}^{z;y}$ originates from the spin magnetization induced by the coupling between the charge-potential gradient along the y direction generated by the applied electric field and the Zeeman interaction. Its θ dependence is given by

$$\alpha_{\rm Z}^{z;y} \propto \cos\frac{\theta}{2}. \tag{45}$$

Accordingly, the angular dependence obtained in Fig. 7(a) can be understood as a result of the increased gain of the charge-potential gradient along the y direction when the apex angle becomes sharper.

In addition, the difference in physical mechanisms between the magnetic- and nonmagnetic-driven ME responses results in distinct size dependence. Figure 7(c) shows the V-shaped lattice size N dependence of the nonmagnetic-driven ME tensor $\alpha^{z;x}$ and the ferromagnetic-driven ME tensor $\alpha_{\rm T}^{z;y}$ in the s-p model. The former $\alpha^{z;x}$, originating from local orbital magnetization and effective spin-orbit interaction, decreases with increasing system size. In contrast, the latter $\alpha_{\rm T}^{z;y}$, which arises from the coupling between the charge-potential gradient and the Zeeman interaction acting over the entire system, increases proportionally with system size. Taking into account that a constant electric field is applied, this calculation of the magnetic-driven ME effect demonstrates that the induced magnetization is proportional to the applied voltage along the y direction.

VII. SUMMARY

In summary, we have theoretically investigated the shape dependence of both nonmagnetic- and magnetic-driven ME responses in the noncentrosymmetric V-shaped chain model. The key advances of this work are threefold: (1) the identification of the characteristic angular dependence of the ME response originating from the interplay between orbital motion and electric polarization in the V-shaped geometry, (2) the characterization of local geometric effects through a scattering-theoretical analysis, and (3) the identification of the dominant microscopic contributions to the ME response using the multipole representation.

To demonstrate these points, we first evaluated the shape dependence of the nonmagnetic-driven ME effect numerically based on the Kubo formula in a model including s and p orbitals. As a result, the magnitude of the ME effect reaches its maximum at an apex angle of $\theta \approx 0.6\pi$. To clarify the origin of the shape dependence, we subsequently performed a detailed theoretical analysis of the numerical results. We then constructed a low-energy effective Hamiltonian by projecting onto the s-orbital basis. Consequently, we found that the polarity induced by the V-shaped geometry manifests as an effective spin-orbit interaction. Furthermore, by analyzing the shape dependence of the Green's function, we clarified that the geometric effect is described by a T-matrix contribution to the Green's function.

Next, we analyzed the selection rules using the multipole basis. It was revealed that the effective spin-orbit interaction and the orbital angular momentum generated by the motion across the apex angle play an essential role in the ME effect. We also found that the term with angle dependence of $\sin\theta \sin\theta/2$, which exhibits a maximum at $\theta = 2\tan^{-1}\sqrt{2} \approx 0.608\pi$, is dominant.

Finally, we also investigated the V-shaped ferromagnetic model including the Zeeman interaction. We found that the magnetic-driven ME response originates from the spin magnetization induced by the coupling between the charge-potential gradient along the y direction generated by the applied electric field and the Zeeman interaction. The difference in physical mechanisms results in distinct shape and size dependence.

Our results clarify the microscopic mechanisms underlying the shape-dependent ME responses in the finite V-shaped chain. In particular, the scattering-theoretical analysis allows us to characterize the effects of local geometric symmetry breaking in terms of the T-matrix, while the multipole representation helps identify the dominant microscopic contributions to the response. The predicted angular dependence may be experimentally examined in suitable V-shaped nanostructures.

These findings highlight the potential of nanoscale geometric design for controlling electronic responses through local symmetry breaking and effective spin-orbit interactions. In realistic nano- and mesoscopic structures, additional effects, such as plasmonic excitations and local electromagnetic fields, may also play important roles in determining their response properties [13,14,30,31]. Investigating the interplay between these effects and the microscopic mechanisms identified in this work is an interesting direction for future research.

Furthermore, the microscopic mechanism of the ME effect discussed in this work may provide insights into bulk systems such as zigzag chain systems, where local inversion symmetry is broken and a variety of odd-parity multipole physics are expected [55,79–83] (e.g., $CeRu_2Al_{10}$ [84,85], Ce_3TiBi_5 [86,87], α-$YbAl_{1-x}Mn_xB_4$ [88], and $NdRu_2Al_{10}$ [89]). Although the present analysis focuses on a finite V-shaped chain, further investigation is required to clarify its applicability to periodic bulk systems.

ACKNOWLEDGMENTS

This research was supported by JST SPRING (Grant No. JPMJSP2119), JST BOOST (Grant No. JPMJBS2426), JSPS KAKENHI (Grants No. JP22H00101, No. JP22H01183, No. JP23H04869, and No. JP23K03288), JST CREST (Grant No. JPMJCR23O4), and JST FOREST (Grant No. JPMJFR2366).

DATA AVAILABILITY

The data that support the findings of this article are openly available in Zenodo [90].

APPENDIX A: GREEN'S FUNCTION OF SIMPLE 1D CHAIN

When $\theta = \pi$, the V-shaped 1D chain represented by Eq. (2) corresponds to a simple 1D chain. Here, we consider the nonmagnetic case for simplicity. The Hamiltonian matrix

$$\bar{h}^{(\pi)} = \bar{h}_{\rm eff}(z+\mu/\hbar)\big|_{\theta=\pi} \tag{A1}$$

can be expressed as $(2N+1)\times(2N+1)$ matrix for the $2N+1$ sites except for the spin degree of freedom:

$$\bar{h}^{(\pi)} = \bar{h}_0 + \bar{h}_{\rm edge}, \tag{A2}$$

$$\bar{h}_0 = \begin{pmatrix} \varepsilon_0 - t_2 & t_1 & t_2 & 0 & 0 & \cdots & 0 & 0 & 0 \\ t_1 & \varepsilon_0 & t_1 & t_2 & 0 & \cdots & 0 & 0 & 0 \\ t_2 & t_1 & \varepsilon_0 & t_1 & t_2 & \cdots & 0 & 0 & 0 \\ 0 & t_2 & t_1 & \varepsilon_0 & t_1 & \cdots & 0 & 0 & 0 \\ 0 & 0 & t_2 & t_1 & \varepsilon_0 & \cdots & 0 & 0 & 0 \\ \vdots & \vdots & \vdots & \vdots & \vdots & \ddots & \vdots & \vdots & \vdots \\ 0 & 0 & 0 & 0 & 0 & \cdots & \varepsilon_0 & t_1 & t_2 \\ 0 & 0 & 0 & 0 & 0 & \cdots & t_1 & \varepsilon_0 & t_1 \\ 0 & 0 & 0 & 0 & 0 & \cdots & t_2 & t_1 & \varepsilon_0 - t_2 \end{pmatrix},$$

$$\bar{h}_{\rm edge} = \begin{pmatrix} 2t_2 & 0 & 0 & \cdots & 0 & 0 & 0 \\ 0 & 0 & 0 & \cdots & 0 & 0 & 0 \\ 0 & 0 & 0 & \cdots & 0 & 0 & 0 \\ \vdots & \vdots & \vdots & \ddots & \vdots & \vdots & \vdots \\ 0 & 0 & 0 & \cdots & 0 & 0 & 0 \\ 0 & 0 & 0 & \cdots & 0 & 0 & 0 \\ 0 & 0 & 0 & \cdots & 0 & 0 & 2t_2 \end{pmatrix}, \tag{A3}$$

where

$$\varepsilon_0 = 2u(z+\mu/\hbar), \quad t_1 = -t_{ss\sigma}, \quad t_2 = -u(z+\mu/\hbar). \tag{A4}$$

By diagonalizing $\bar{h}_0$, the eigenenergies $E^{(0)}_{k_m}$ and the eigenstates $\psi^{(0)}_{k_m}(R^x_n)$ are obtained as follows:

$$E^{(0)}_{k_m} = \varepsilon_0 + 2t_1\cos(k_m a) + 2t_2\cos(2k_m a), \tag{A5a}$$

$$\psi^{(0)}_{k_m}\left(R^x_n\right) = \begin{cases} \sqrt{\dfrac{2a}{L}}\sin\left(k_m R^x_n\right) & (m = \text{even}), \\ \sqrt{\dfrac{2a}{L}}\cos\left(k_m R^x_n\right) & (m = \text{odd}), \end{cases} \tag{A5b}$$

where $L = (2N+2)a$,

$$k_m = \frac{\pi}{L}m \quad (m = 1, 2, \ldots, 2N+1). \tag{A6}$$

Therefore, the Green's function of $\bar{h}_0$ is given as follows:

$$[\bar{\mathcal{G}}_0(z)]^{mn'}_{\sigma\sigma'} = \sum_{k_m} \frac{\psi^{(0)}_{k_m}\left(R^x_n\right)\psi^{(0)*}_{k_m}\left(R^x_{n'}\right)}{\hbar z + \mu - E^{(0)}_{k_m}}[\bar{\sigma}_0]_{\sigma\sigma'}. \tag{A7}$$

Then, the Green's function of $\bar{h}^{(\pi)}$ is obtained from the Dyson equation:

$$\bar{\mathcal{G}}^{(\pi)}_{\rm eff} = \bar{\mathcal{G}}_0 + \bar{\mathcal{G}}_0 \bar{h}_{\rm edge} \bar{\mathcal{G}}^{(\pi)}_{\rm eff}. \tag{A8}$$

Solving this equation, we obtain

$$\bar{\mathcal{G}}^{(\pi)}_{\rm eff} = \bar{\mathcal{G}}_0 + \bar{\mathcal{G}}_0 \bar{h}_{\rm edge} \frac{1}{1 - \bar{\mathcal{G}}_0 \bar{h}_{\rm edge}} \bar{\mathcal{G}}_0. \tag{A9}$$

APPENDIX B: MATRIX REPRESENTATION OF MULTIPOLES

We show the matrix elements of the multipole operators [23,24,26,75]. The on-site and real bond degrees of freedom are described by electric multipoles $\bar{q}^{\rm c}$ and $\bar{q}^{{\rm b}n}$ and the imaginary bond degrees of freedom are described by magnetic toroidal multipoles $\bar{t}^{{\rm b}n}$. As an example, for the seven-site basis ($N = 3$), the relevant matrix elements of the multipoles are given as follows:

$$\bar{q}^{\rm c}_0 = \begin{pmatrix} 1&0&0&0&0&0&0\\ 0&1&0&0&0&0&0\\ 0&0&1&0&0&0&0\\ 0&0&0&1&0&0&0\\ 0&0&0&0&1&0&0\\ 0&0&0&0&0&1&0\\ 0&0&0&0&0&0&1 \end{pmatrix}, \quad \bar{q}^{\rm b1}_0 = \begin{pmatrix} 0&1&0&0&0&0&0\\ 1&0&1&0&0&0&0\\ 0&1&0&1&0&0&0\\ 0&0&1&0&1&0&0\\ 0&0&0&1&0&1&0\\ 0&0&0&0&1&0&1\\ 0&0&0&0&0&1&0 \end{pmatrix},$$

$$\bar{q}^{\rm b2}_0 = \begin{pmatrix} 0&0&1&0&0&0&0\\ 0&0&0&1&0&0&0\\ 1&0&0&0&1&0&0\\ 0&1&0&0&0&1&0\\ 0&0&1&0&0&0&1\\ 0&0&0&1&0&0&0\\ 0&0&0&0&1&0&0 \end{pmatrix}, \ldots, \quad \bar{q}^{\rm c\prime}_0 = \begin{pmatrix} 0&0&0&0&0&0&0\\ 0&0&0&0&0&0&0\\ 0&0&1&0&0&0&0\\ 0&0&0&0&0&0&0\\ 0&0&0&0&1&0&0\\ 0&0&0&0&0&0&0\\ 0&0&0&0&0&0&0 \end{pmatrix},$$

$$\bar{q}^{\rm b2\prime}_0 = \begin{pmatrix} 0&0&0&0&0&0&0\\ 0&0&0&0&0&0&0\\ 0&0&0&0&1&0&0\\ 0&0&0&0&0&0&0\\ 0&0&1&0&0&0&0\\ 0&0&0&0&0&0&0\\ 0&0&0&0&0&0&0 \end{pmatrix}, \quad \bar{t}^{\rm b2\prime}_x = \begin{pmatrix} 0&0&0&0&0&0&0\\ 0&0&0&0&0&0&0\\ 0&0&0&0&-i&0&0\\ 0&0&0&0&0&0&0\\ 0&0&i&0&0&0&0\\ 0&0&0&0&0&0&0\\ 0&0&0&0&0&0&0 \end{pmatrix},$$

$$\bar{q}^{\rm c}_x = \begin{pmatrix} -3&0&0&0&0&0&0\\ 0&-2&0&0&0&0&0\\ 0&0&-1&0&0&0&0\\ 0&0&0&0&0&0&0\\ 0&0&0&0&1&0&0\\ 0&0&0&0&0&2&0\\ 0&0&0&0&0&0&3 \end{pmatrix}, \quad \bar{q}^{\rm c}_y = \begin{pmatrix} 3&0&0&0&0&0&0\\ 0&2&0&0&0&0&0\\ 0&0&1&0&0&0&0\\ 0&0&0&0&0&0&0\\ 0&0&0&0&1&0&0\\ 0&0&0&0&0&2&0\\ 0&0&0&0&0&0&3 \end{pmatrix}. \tag{B1}$$

We display schematic pictures of the multipole bases $\bar{q}^{\rm c}_0$, $\bar{q}^{\rm b1}_0$, $\bar{q}^{\rm b2\prime}_0$, $\bar{t}^{\rm b2\prime}_x$, $\bar{q}^{\rm c}_x$, $\bar{q}^{\rm c}_y$, and $\bar{\sigma}_\nu$ ($\nu = x, y, z$) in Fig. 8.

APPENDIX C: MULTIPOLE-BASIS REPRESENTATION OF THE ME TENSOR

We present the expressions for the ME tensor decomposed in the multipole basis, corresponding to Figs. 5 and 7(b). By separating the θ dependence of each operator in the definition of $\alpha^{zx}_{\rm eff}$ in

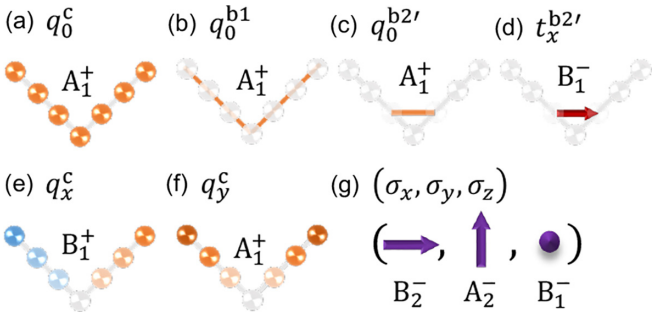


FIG. 8. Schematic pictures of the multipole basis for the cluster, bond, and spin for the seven-site basis [(a)–(g)] together with the corresponding irreducible representations under the point group C_{2v}. The superscript $\pm$ of the irreducible representation denotes the parity with respect to the time-reversal operation.

Eq. (24), we obtain the following:

$$\begin{aligned}
\alpha_{\rm eff}^{z;x}(i\omega_m) &= -\frac{k_{\rm B}T}{V}\sum_{i\epsilon_n}{\rm Tr}\big[\big(\bar{M}_{\rm eff}^{z(\pi)}+\Delta\bar{M}_{\rm eff}^{z(\theta)}\big)\big(\bar{\mathcal{G}}^{+}+\bar{\mathcal{G}}^{+}\bar{\mathcal{T}}^{(\theta)+}\bar{\mathcal{G}}^{+}\big)\bar{P}^{x}\big(\bar{\mathcal{G}}+\bar{\mathcal{G}}\bar{\mathcal{T}}^{(\theta)}\bar{\mathcal{G}}\big)\big]\\
&= -\frac{k_{\rm B}T}{V}\sum_{i\epsilon_n}{\rm Tr}\big[\big(M_{q_0^{\rm c}\sigma_z}\big(\bar{q}_0^{\rm c}\bar{\sigma}_z\big)+M_{q_0^{\rm b}\sigma_z}\big(\bar{q}_0^{\rm b2}\bar{\sigma}_z\big)+\Delta M_{q_0^{\rm b}\sigma_z}\big(\bar{q}_0^{\rm b2'}\bar{\sigma}_z\big)+\Delta M_{t_x^{\rm b}\sigma_0}\big(\bar{t}_x^{\rm b2'}\bar{\sigma}_0\big)\big)\\
&\quad\times\big(\bar{\mathcal{G}}^{+}+\bar{\mathcal{G}}^{+}\big[\mathcal{T}^{+}_{q_0^{\rm c}\sigma_0}\big(\bar{q}_0^{\rm c'}\bar{\sigma}_0\big)+\mathcal{T}^{+}_{q_0^{\rm b}\sigma_0}\big(\bar{q}_0^{\rm b2'}\bar{\sigma}_0\big)+\mathcal{T}^{+}_{t_x^{\rm b}\sigma_0}\big(\bar{t}_x^{\rm b2'}\bar{\sigma}_z\big)\big]\bar{\mathcal{G}}^{+}\big)\\
&\quad\times\big(P_{q_x^{\rm c}\sigma_0}\big(\bar{q}_x^{\rm c}\bar{\sigma}_0\big)\big)\times\big(\bar{\mathcal{G}}+\bar{\mathcal{G}}\big[\mathcal{T}_{q_0^{\rm c}\sigma_0}\big(\bar{q}_0^{\rm c'}\bar{\sigma}_0\big)+\mathcal{T}_{q_0^{\rm b}\sigma_0}\big(\bar{q}_0^{\rm b2'}\bar{\sigma}_0\big)+\mathcal{T}_{t_x^{\rm b}\sigma_0}\big(\bar{t}_x^{\rm b2'}\bar{\sigma}_z\big)\big]\bar{\mathcal{G}}\big)\big]\\
&= \alpha_{\rm i}^{z;x}+\alpha_{\rm ii}^{z;x}+\alpha_{\rm iii}^{z;x}+\alpha_{\rm iv}^{z;x}+O\big(\Delta_p^{-4}\big),
\end{aligned}\tag{C1}$$

where $\bar{\mathcal{G}}$ stands for the simple 1D chain Green's function with $\theta=\pi$, the superscript "+" on the Green's function and the T-matrix indicates that their frequency arguments are $i\epsilon_n+i\omega_m$ [e.g., $\bar{\mathcal{G}}^{+}=\bar{\mathcal{G}}(i\epsilon_n+i\omega_m)$]. $\mathcal{T}_{q_0^{\rm c}\sigma_0}$, $\mathcal{T}_{q_0^{\rm b}\sigma_0}$, $\mathcal{T}_{t_x^{\rm b}\sigma_z}$ $\Delta M_{q_0^{\rm b}\sigma_z}$, and $\Delta M_{t_x^{\rm b}\sigma_0}$ are the components of the T-matrix and the effective magnetization defined in Eqs. (33) and (35). $M_{q_0^{\rm c}\sigma_z}$, $M_{q_0^{\rm b}\sigma_z}$, $P_{q_x^{\rm c}\sigma_0}$, and $P_{q_y^{\rm c}\sigma_0}$ denote the $\theta=\pi$ components of the effective magnetization and the electric polarization operators along the x and y directions, respectively. Their expressions are given by

$$\begin{aligned}
&M_{q_0^{\rm c}\sigma_z}=\frac{a}{2V}{\rm Tr}\big[\,\big(\bar{q}_0^{\rm c}\bar{\sigma}_z\big)\,\bar{M}_{\rm eff}^{z(\pi)}\,\big],\quad M_{q_0^{\rm b}\sigma_z}=\frac{a}{2V}{\rm Tr}\big[\,\big(\bar{q}_0^{\rm b2}\bar{\sigma}_z\big)\,\bar{M}_{\rm eff}^{z(\pi)}\,\big],\\
&P_{q_x^{\rm c}\sigma_0}=a\sin\frac{\theta}{2},\quad P_{q_y^{\rm c}\sigma_0}=a\cos\frac{\theta}{2}.
\end{aligned}\tag{C2}$$

Equation (44) of $\alpha_{\rm eff}^{z;y}$ can also be obtained through a similar expansion.

With the condition ${\rm Tr}[*]\neq 0$ in mind, and using Eq. (39), $\alpha_{\rm i}^{z;x}$, $\alpha_{\rm ii}^{z;x}$, $\alpha_{\rm iii}^{z;x}$, $\alpha_{\rm iv}^{z;x}$, and $\alpha_{\rm Z}^{z;y}$ are given as follows:

$$\alpha_{\rm i}^{z;x}=-\frac{k_{\rm B}T}{V}\sum_{i\epsilon_n}{\rm Tr}\big[\,\big(\bar{t}_x^{\rm b2'}\bar{\sigma}_0\big)\,\bar{\mathcal{G}}^{+}\,\big(\bar{q}_x^{\rm c}\bar{\sigma}_0\big)\,\bar{\mathcal{G}}\,\big]\Delta M_{t_x^{\rm b}\sigma_0}P_{q_x^{\rm c}\sigma_0},\tag{C3a}$$

$$\begin{aligned}
\alpha_{\rm ii}^{z;x}&=-\frac{k_{\rm B}T}{V}\sum_{i\epsilon_n}{\rm Tr}\big[\,\big(\bar{t}_x^{\rm b2'}\bar{\sigma}_0\big)\,\bar{\mathcal{G}}^{+}\,\big(\bar{q}_x^{\rm c}\bar{\sigma}_0\big)\,\bar{\mathcal{G}}\,\big(\bar{q}_0^{\rm b2'}\bar{\sigma}_0\big)\,\bar{\mathcal{G}}\,\big]\Delta M_{t_x^{\rm b}\sigma_0}P_{q_x^{\rm c}\sigma_0}\mathcal{T}_{q_0^{\rm b}\sigma_0}\\
&\quad-\frac{k_{\rm B}T}{V}\sum_{i\epsilon_n}{\rm Tr}\big[\,\big(\bar{t}_x^{\rm b2'}\bar{\sigma}_0\big)\,\bar{\mathcal{G}}^{+}\,\big(\bar{q}_0^{\rm b2'}\bar{\sigma}_0\big)\,\bar{\mathcal{G}}^{+}\,\big(\bar{q}_x^{\rm c}\bar{\sigma}_0\big)\,\bar{\mathcal{G}}\,\big]\Delta M_{t_x^{\rm b}\sigma_0}\mathcal{T}^{+}_{q_0^{\rm b}\sigma_0}P_{q_x^{\rm c}\sigma_0},
\end{aligned}\tag{C3b}$$

$$\alpha^{z;x}_{\mathrm{iii}} = -\frac{k_{\mathrm{B}}T}{V}\sum_{i\epsilon_n}\mathrm{Tr}\big[\,(\bar{q}^{\mathrm{c}}_0\bar{\sigma}_z)\,\bar{\mathcal{G}}^{+}\,(\bar{q}^{\mathrm{c}}_x\bar{\sigma}_0)\,\bar{\mathcal{G}}\,(\bar{t}^{\mathrm{b}2\prime}_x\bar{\sigma}_z)\,\bar{\mathcal{G}}\,\big]M_{q^{\mathrm{c}}_0\sigma_z}P_{q^{\mathrm{c}}_x\sigma_0}\mathcal{T}_{t^{\mathrm{b}}_x\sigma_z}$$
$$-\frac{k_{\mathrm{B}}T}{V}\sum_{i\epsilon_n}\mathrm{Tr}\big[\,(\bar{q}^{\mathrm{c}}_0\bar{\sigma}_z)\,\bar{\mathcal{G}}^{+}\,(\bar{t}^{\mathrm{b}2\prime}_x\bar{\sigma}_z)\,\bar{\mathcal{G}}^{+}\,(\bar{q}^{\mathrm{c}}_x\bar{\sigma}_0)\,\bar{\mathcal{G}}\,\big]M_{q^{\mathrm{c}}_0\sigma_z}\mathcal{T}^{+}_{t^{\mathrm{b}}_x\sigma_z}P_{q^{\mathrm{c}}_x\sigma_0}, \tag{C3c}$$

$$\alpha^{z;x}_{\mathrm{iv}} = -\frac{k_{\mathrm{B}}T}{V}\sum_{i\epsilon_n}\mathrm{Tr}\big[\,(\bar{q}^{\mathrm{c}}_0\bar{\sigma}_0)\,\bar{\mathcal{G}}^{+}\,(\bar{q}^{\mathrm{b}2\prime}_0\bar{\sigma}_z)\,\bar{\mathcal{G}}^{+}\,(\bar{q}^{\mathrm{c}}_x\bar{\sigma}_0)\,\bar{\mathcal{G}}\,(\bar{t}^{\mathrm{b}2\prime}_x\bar{\sigma}_z)\,\bar{\mathcal{G}}\,\big]M_{q^{\mathrm{c}}_0\sigma_z}\mathcal{T}^{+}_{q^{\mathrm{b}}_0\sigma_0}P_{q^{\mathrm{c}}_x\sigma_0}\mathcal{T}_{t^{\mathrm{b}}_x\sigma_z}$$
$$-\frac{k_{\mathrm{B}}T}{V}\sum_{i\epsilon_n}\mathrm{Tr}\big[\,(\bar{q}^{\mathrm{c}}_0\bar{\sigma}_0)\,\bar{\mathcal{G}}^{+}\,(\bar{t}^{\mathrm{b}2\prime}_x\bar{\sigma}_z)\,\bar{\mathcal{G}}^{+}\,(\bar{q}^{\mathrm{c}}_x\bar{\sigma}_0)\,\bar{\mathcal{G}}\,(\bar{q}^{\mathrm{b}2\prime}_0\bar{\sigma}_z)\,\bar{\mathcal{G}}\,\big]M_{q^{\mathrm{c}}_0\sigma_z}\mathcal{T}^{+}_{t^{\mathrm{b}}_x\sigma_z}P_{q^{\mathrm{c}}_x\sigma_0}\mathcal{T}_{q^{\mathrm{b}}_0\sigma_0}, \tag{C3d}$$

$$\alpha^{z;y}_{\mathrm{Z}} = -\frac{k_{\mathrm{B}}T}{V}\sum_{i\epsilon_n}\mathrm{Tr}\big[\,(\bar{q}^{\mathrm{c}}_0\bar{\sigma}_0)\,\bar{\mathcal{G}}^{+}\,(\bar{q}^{\mathrm{c}}_y\bar{\sigma}_0)\,\bar{\mathcal{G}}\,\big]M_{q^{\mathrm{c}}_0\sigma_z}P_{q^{\mathrm{c}}_y\sigma_0}. \tag{C3e}$$

From these equations, the θ and Δ_p dependence of the ME tensor in Eqs. (41) and (45) is obtained.

[1] W. Cai, U. K. Chettiar, A. V. Kildishev, and V. M. Shalaev, Optical cloaking with metamaterials, Nat. Photon. **1**, 224 (2007).

[2] C. M. Soukoulis and M. Wegener, Optical metamaterials—More bulky and less lossy, Science **330**, 1633 (2010).

[3] C. M. Soukoulis and M. Wegener, Past achievements and future challenges in the development of three-dimensional photonic metamaterials, Nat. Photon. **5**, 523 (2011).

[4] N. I. Zheludev and Y. S. Kivshar, From metamaterials to metadevices, Nat. Mater. **11**, 917 (2012).

[5] H.-H. Hsiao, C. H. Chu, and D. P. Tsai, Fundamentals and applications of metasurfaces, Small Methods **1**, 1600064 (2017).

[6] M. Matsubara, T. Kobayashi, H. Watanabe, Y. Yanase, S. Iwata, and T. Kato, Polarization-controlled tunable directional spin-driven photocurrents in a magnetic metamaterial with threefold rotational symmetry, Nat. Commun. **13**, 6708 (2022).

[7] M. Hild, L. E. Golub, A. Fuhrmann, M. Otteneder, M. Kronseder, M. Matsubara, T. Kobayashi, D. Oshima, A. Honda, T. Kato, J. Wunderlich, C. Back, and S. D. Ganichev, Terahertz spin ratchet effect in magnetic metamaterials, Phys. Rev. B **107**, 155419 (2023).

[8] G. Cavanna, H. Taketani, H. Watanabe, D. Pan, A. Honda, D. Oshima, T. Kato, and M. Matsubara, Scaling-dependent tunability of spin-driven photocurrents in magnetic metamaterials, Nanophotonics **14**, 5611 (2025).

[9] M. Kuwata-Gonokami, N. Saito, Y. Ino, M. Kauranen, K. Jefimovs, T. Vallius, J. Turunen, and Y. Svirko, Giant optical activity in quasi-two-dimensional planar nanostructures, Phys. Rev. Lett. **95**, 227401 (2005).

[10] N. Yu, P. Genevet, M. A. Kats, F. Aieta, J.-P. Tetienne, F. Capasso, and Z. Gaburro, Light propagation with phase discontinuities: Generalized laws of reflection and refraction, Science **334**, 333 (2011).

[11] J. C. Gartside, A. Vanstone, T. Dion, K. D. Stenning, D. M. Arroo, H. Kurebayashi, and W. R. Branford, Reconfigurable magnonic mode-hybridisation and spectral control in a bicomponent artificial spin ice, Nat. Commun. **12**, 2488 (2021).

[12] D. Sekine, Y. Sato, and M. Matsubara, Nonlinear optical detection of mesoscopic magnetic toroidal dipoles, Appl. Phys. Lett. **120**, 162905 (2022).

[13] S. Link, M. B. Mohamed, and M. A. El-Sayed, Simulation of the optical absorption spectra of gold nanorods as a function of their aspect ratio and the effect of the medium dielectric constant, J. Phys. Chem. B **103**, 3073 (1999).

[14] P. K. Jain, K. S. Lee, I. H. El-Sayed, and M. A. El-Sayed, Calculated absorption and scattering properties of gold nanoparticles of different size, shape, and composition: Applications in biological imaging and biomedicine, J. Phys. Chem. B **110**, 7238 (2006).

[15] J. Cai, P. Ruffieux, R. Jaafar, M. Bieri, T. Braun, S. Blankenburg, M. Muoth, A. P. Seitsonen, M. Saleh, X. Feng, K. Müllen, and R. Fasel, Atomically precise bottom-up fabrication of graphene nanoribbons, Nature (London) **466**, 470 (2010).

[16] Y. Cao, V. Fatemi, A. Demir, S. Fang, S. L. Tomarken, J. Y. Luo, J. D. Sanchez-Yamagishi, K. Watanabe, T. Taniguchi, E. Kaxiras, R. C. Ashoori, and P. Jarillo-Herrero, Correlated insulator behaviour at half-filling in magic-angle graphene superlattices, Nature (London) **556**, 80 (2018).

[17] R. S. K. Houtsma, J. de la Rie, and M. Stöhr, Atomically precise graphene nanoribbons: Interplay of structural and electronic properties, Chem. Soc. Rev. **50**, 6541 (2021).

[18] S. Hayami and H. Kusunose, Microscopic description of electric and magnetic toroidal multipoles in hybrid orbitals, J. Phys. Soc. Jpn. **87**, 033709 (2018).

[19] S. Hayami, M. Yatsushiro, Y. Yanagi, and H. Kusunose, Classification of atomic-scale multipoles under crystallographic point groups and application to linear response tensors, Phys. Rev. B **98**, 165110 (2018).

[20] H. Watanabe and Y. Yanase, Group-theoretical classification of multipole order: Emergent responses and candidate materials, Phys. Rev. B **98**, 245129 (2018).

[21] M. Yatsushiro, H. Kusunose, and S. Hayami, Multipole classification in 122 magnetic point groups for unified understanding of multiferroic responses and transport phenomena, Phys. Rev. B **104**, 054412 (2021).

[22] H. Kusunose and S. Hayami, Generalization of microscopic multipoles and cross-correlated phenomena by their orderings, J. Phys.: Condens. Matter **34**, 464002 (2022).

[23] R. Oiwa and H. Kusunose, Systematic analysis method for nonlinear response tensors, J. Phys. Soc. Jpn. **91**, 014701 (2022).

[24] S. Hayami and H. Kusunose, Unified description of electronic orderings and cross correlations by complete multipole representation, J. Phys. Soc. Jpn. **93**, 072001 (2024).

[25] H. Kusunose, R. Oiwa, and S. Hayami, Complete multipole basis set for single-centered electron systems, J. Phys. Soc. Jpn. **89**, 104704 (2020).

[26] S. Hayami, Y. Yanagi, and H. Kusunose, Bottom-up design of spin-split and reshaped electronic band structures in antiferromagnets without spin-orbit coupling: Procedure on the basis of augmented multipoles, Phys. Rev. B **102**, 144441 (2020).

[27] X. Gao, X. Han, W.-P. Cao, H. O. Li, H. F. Ma, and T. J. Cui, Ultrawideband and high-efficiency linear polarization converter based on double V-shaped metasurface, IEEE Trans. Antennas Propag. **63**, 3522 (2015).

[28] Y. Xie, C. Yang, Y. Wang, Y. Shen, X. Deng, B. Zhou, and J. Cao, Anomalous refraction and reflection characteristics of bend V-shaped antenna metasurfaces, Sci. Rep. **9**, 6700 (2019).

[29] J. Hu, S. Bandyopadhyay, Y.-H. Liu, and L.-Y. Shao, A review on metasurface: From principle to smart metadevices, Front. Phys. **8**, 586087 (2021).

[30] L. Billot, M. Mortier, and L. Aigouy, Near-field observation of surface plasmon polaritons launched by V-shaped nanorods on a gold surface, Appl. Opt. **54**, 9326 (2015).

[31] A. Babynina, M. Fedoruk, P. Kühler, A. Meledin, M. Döblinger, and T. Lohmüller, Bending gold nanorods with light, Nano Lett. **16**, 6485 (2016).

[32] V. Edelstein, Spin polarization of conduction electrons induced by electric current in two-dimensional asymmetric electron systems, Solid State Commun. **73**, 233 (1990).

[33] T. Furukawa, Y. Shimokawa, K. Kobayashi, and T. Itou, Observation of current-induced bulk magnetization in elemental tellurium, Nat. Commun. **8**, 954 (2017).

[34] R. González-Hernández, P. Ritzinger, K. Výborný, J. Železný, and A. Manchon, Non-relativistic torque and Edelstein effect in non-collinear magnets, Nat. Commun. **15**, 7663 (2024).

[35] A. Popoola, R. Kashikar, A. Azmy, I. Spanopoulos, H. Jafari, J. Sławińska, S. Witanachchi, S. Lisenkov, and I. Ponomareva, Mechanically and electrically tunable Rashba-Edelstein effect in ferroelectric semiconductors, $CsGeX_3$ ($X = \mathrm{I},\ \mathrm{Br},\ \mathrm{Cl}$), Phys. Rev. Mater. **9**, 084412 (2025).

[36] I. Sodemann and L. Fu, Quantum nonlinear Hall effect induced by Berry curvature dipole in time-reversal invariant materials, Phys. Rev. Lett. **115**, 216806 (2015).

[37] L. Xu, M. Yang, S. J. Wang, and Y. P. Feng, Electronic and optical properties of the monolayer group-IV monochalcogenides MX ($M = \mathrm{Ge},\ \mathrm{Sn}$; $X = \mathrm{S},\ \mathrm{Se},\ \mathrm{Te}$), Phys. Rev. B **95**, 235434 (2017).

[38] Q. Ma, S.-Y. Xu, H. Shen, D. MacNeill, V. Fatemi, T.-R. Chang, A. M. Mier Valdivia, S. Wu, Z. Du, C.-H. Hsu, *et al.*, Observation of the nonlinear Hall effect under time-reversal-symmetric conditions, Nature (London) **565**, 337 (2019).
[39] H. Wang and X. Qian, Ferroelectric nonlinear anomalous Hall effect in few-layer WTe_2, npj Comput. Mater. **5**, 119 (2019).
[40] M. Nakamura, S. Horiuchi, F. Kagawa, N. Ogawa, T. Kurumaji, Y. Tokura, and M. Kawasaki, Shift current photovoltaic effect in a ferroelectric charge-transfer complex, Nat. Commun. **8**, 281 (2017).
[41] N. Ogawa, M. Sotome, Y. Kaneko, M. Ogino, and Y. Tokura, Shift current in the ferroelectric semiconductor SbSI, Phys. Rev. B **96**, 241203(R) (2017).
[42] D. Shin, S. A. Sato, H. Hübener, U. De Giovannini, N. Park, and A. Rubio, Dynamical amplification of electric polarization through nonlinear phononics in 2D SnTe, npj Comput. Mater. **6**, 182 (2020).
[43] M. S. Okyay, S. A. Sato, K. W. Kim, B. Yan, H. Jin, and N. Park, Second harmonic Hall responses of insulators as a probe of Berry curvature dipole, Commun. Phys. **5**, 303 (2022).
[44] R. Resta and D. Vanderbilt, Theory of polarization: A modern approach, in *Physics of Ferroelectrics: A Modern Perspective* (Springer, Berlin, 2007), pp. 31–68.
[45] C. Cui, F. Xue, W.-J. Hu, and L.-J. Li, Two-dimensional materials with piezoelectric and ferroelectric functionalities, npj 2D Mater. Appl. **2**, 18 (2018).
[46] Y. Poplavko, Piezoelectric intrinsic polarity modeling and determination, APL Mater. **13**, 061113 (2025).
[47] V. Dubovik and V. Tugushev, Toroid moments in electrodynamics and solid-state physics, Phys. Rep. **187**, 145 (1990).
[48] N. A. Spaldin, M. Fiebig, and M. Mostovoy, The toroidal moment in condensed-matter physics and its relation to the magnetoelectric effect, J. Phys.: Condens. Matter **20**, 434203 (2008).
[49] Y. V. Kopaev, Toroidal ordering in crystals, Phys. Usp. **52**, 1111 (2009).
[50] M. Fiebig, Revival of the magnetoelectric effect, J. Phys. D: Appl. Phys. **38**, R123 (2005).
[51] S. Hayami, H. Kusunose, and Y. Motome, Emergent spin-valley-orbital physics by spontaneous parity breaking, J. Phys.: Condens. Matter **28**, 395601 (2016).
[52] H. Saito, K. Uenishi, N. Miura, C. Tabata, H. Hidaka, T. Yanagisawa, and H. Amitsuka, Evidence of a new current-induced magnetoelectric effect in a toroidal magnetic ordered state of UNi_4B, J. Phys. Soc. Jpn. **87**, 033702 (2018).
[53] Y. Gao, D. Vanderbilt, and D. Xiao, Microscopic theory of spin toroidization in periodic crystals, Phys. Rev. B **97**, 134423 (2018).
[54] L. Ding, X. Xu, H. O. Jeschke, X. Bai, E. Feng, A. S. Alemayehu, J. Kim, F.-T. Huang, Q. Zhang, X. Ding, N. Harrison, V. Zapf, D. Khomskii, I. I. Mazin, S.-W. Cheong, and H. Cao, Field-tunable toroidal moment in a chiral-lattice magnet, Nat. Commun. **12**, 5339 (2021).
[55] M. Yatsushiro, R. Oiwa, H. Kusunose, and S. Hayami, Analysis of model-parameter dependences on the second-order nonlinear conductivity in $\mathcal{PT}$-symmetric collinear antiferromagnetic metals with magnetic toroidal moment on zigzag chains, Phys. Rev. B **105**, 155157 (2022).
[56] A. Kirikoshi and S. Hayami, Finite-q antiferrotoroidal and ferritoroidal order in a distorted kagome structure, Phys. Rev. B **111**, L201112 (2025).
[57] Y. Tokura and N. Nagaosa, Nonreciprocal responses from non-centrosymmetric quantum materials, Nat. Commun. **9**, 3740 (2018).
[58] H. Isobe and N. Nagaosa, Toroidal scattering and nonreciprocal transport by magnetic impurities, J. Phys. Soc. Jpn. **91**, 115001 (2022).
[59] T. Yamanaka, Y. Ihara, and S. Hayami, Nonlinear nonreciprocal electric conductivity driven by magnetic field gradients, J. Phys. Soc. Jpn. **94**, 083705 (2025).
[60] K. Sawada and N. Nagaosa, Optical magnetoelectric effect in multiferroic materials: Evidence for a Lorentz force acting on a ray of light, Phys. Rev. Lett. **95**, 237402 (2005).
[61] S. Miyahara and N. Furukawa, Nonreciprocal directional dichroism and toroidalmagnons in helical magnets, J. Phys. Soc. Jpn. **81**, 023712 (2012).
[62] J. Mund, D. R. Yakovlev, A. N. Poddubny, R. M. Dubrovin, M. Bayer, and R. V. Pisarev, Toroidal nonreciprocity of optical second harmonic generation, Phys. Rev. B **103**, L180410 (2021).

[63] J. C. Slater and G. F. Koster, Simplified LCAO method for the periodic potential problem, Phys. Rev. **94**, 1498 (1954).
[64] A. M. Essin, J. E. Moore, and D. Vanderbilt, Magnetoelectric polarizability and axion electrodynamics in crystalline insulators, Phys. Rev. Lett. **102**, 146805 (2009).
[65] S. Coh, D. Vanderbilt, A. Malashevich, and I. Souza, Chern-Simons orbital magnetoelectric coupling in generic insulators, Phys. Rev. B **83**, 085108 (2011).
[66] K. Tazuke, T. Morimoto, and S. Kitamura, Formulation of the orbital magnetic moment in multi-orbital tight-binding models: Application to the inverse Faraday effect, Phys. Rev. B **112**, 155134 (2025).
[67] P.-O. Löwdin, Studies in perturbation theory. IV. Solution of eigenvalue problem by projection operator formalism, J. Math. Phys. **3**, 969 (1962).
[68] H. Feshbach, Unified theory of nuclear reactions, Rev. Mod. Phys. **36**, 1076 (1964).
[69] J. Leinaas and T. Kuo, Convergence properties of the Brillouin-Wigner type of perturbation expansion, Ann. Phys. **111**, 19 (1978).
[70] N. Hatano and G. Ordonez, Time-reversal symmetric resolution of unity without background integrals in open quantum systems, J. Math. Phys. **55**, 122106 (2014).
[71] A. Altland and B. D. Simons, *Condensed Matter Field Theory*, 2nd ed. (Cambridge University Press, Cambridge, 2010).
[72] J. Ōiké and R. Peters, Impact of electron correlations on the nonlinear Edelstein effect, Phys. Rev. B **110**, 165111 (2024).
[73] B. A. Lippmann and J. Schwinger, Variational principles for scattering processes. I, Phys. Rev. **79**, 469 (1950).
[74] J. L. Beeby, Electronic structure of alloys, Phys. Rev. **135**, A130 (1964).
[75] S. Hayami, Y. Yanagi, H. Kusunose, and Y. Motome, Electric toroidal quadrupoles in the spin-orbit-coupled metal $Cd_2Re_2O_7$, Phys. Rev. Lett. **122**, 147602 (2019).
[76] H. Kusunose, R. Oiwa, and S. Hayami, Symmetry-adapted modeling for molecules and crystals, Phys. Rev. B **107**, 195118 (2023).
[77] R. Oiwa, A. Inda, S. Hayami, T. Nomoto, R. Arita, and H. Kusunose, Symmetry-adapted closest Wannier modeling based on complete multipole basis set, Phys. Rev. B **112**, 035116 (2025).
[78] L. Huang and C. Yue, Barycentric rational function approximation made simple: A fast analytic continuation method for Matsubara Green's functions, Phys. Rev. B **111**, 125139 (2025).
[79] Y. Yanase, Magneto-electric effect in three-dimensional coupled zigzag chains, J. Phys. Soc. Jpn. **83**, 014703 (2014).
[80] S. Hayami, H. Kusunose, and Y. Motome, Spontaneous multipole ordering by local parity mixing, J. Phys. Soc. Jpn. **84**, 064717 (2015).
[81] S. Hayami, H. Kusunose, and Y. Motome, Asymmetric magnon excitation by spontaneous toroidal ordering, J. Phys. Soc. Jpn. **85**, 053705 (2016).
[82] Y. Suzuki, Tunneling spin current in systems with spin degeneracy, Phys. Rev. B **105**, 075201 (2022).
[83] S. Kanda and S. Hayami, Revisiting magnetoelectric response in collinear antiferromagnetic zigzag chains: A downfolding approach beyond conventional low-energy models, Phys. Rev. B **114**, 165141 (2026).
[84] A. I. Tursina, S. N. Nesterenko, E. V. Murashova, I. V. Chernyshev, H. Noël, and Y. D. Seropegin, $CeRu_2Al_{10}$ with the $YbFe_2Al_{10}$ structure type, Acta Crystallogr. E **61**, i12 (2005).
[85] H. Kato, R. Kobayashi, T. Takesaka, T. Nishioka, M. Matsumura, K. Kaneko, and N. Metoki, Magnetic structure determination of CeT_2Al_{10} (T = Ru and Os): Single crystal neutron diffraction studies, J. Phys. Soc. Jpn. **80**, 073701 (2011).
[86] M. Shinozaki, G. Motoyama, T. Mutou, S. Nishigori, A. Yamaguchi, K. Fujiwara, K. Miyoshi, and A. Sumiyama, Study for current-induced magnetization in ferrotoroidal ordered state of Ce_3TiBi_5, JPS Conf. Proc. **30**, 011189 (2020).
[87] M. Shinozaki, G. Motoyama, M. Tsubouchi, M. Sezaki, J. Gouchi, S. Nishigori, T. Mutou, A. Yamaguchi, K. Fujiwara, K. Miyoshi, and Y. Uwatoko, Magnetoelectric effect in the

antiferromagnetic ordered state of Ce_3TiBi_5 with Ce zig-zag chains, J. Phys. Soc. Jpn. **89**, 033703 (2020).

[88] S. Suzuki, K. Takubo, K. Kuga, W. Higemoto, T. U. Ito, T. Tomita, Y. Shimura, Y. Matsumoto, C. Bareille, H. Wadati, S. Shin, and S. Nakatsuji, High-temperature antiferromagnetism in Yb based heavy fermion systems proximate to a Kondo insulator, Phys. Rev. Res. **3**, 023140 (2021).

[89] K. Sudo, Y. Yanagi, M. Akaki, H. Tanida, and M. Kimata, Large spontaneous nonreciprocal charge transport in a zero-magnetization antiferromagnet, Phys. Rev. Lett. **136**, 016503 (2026).

[90] S. Kanda and S. Hayami, Dataset for: "Shape dependence of Edelstein and magnetoelectric effects in the V-shaped model", Zenodo, 2026, 10.5281/zenodo.23495185.